

Evolution of a Surge Cycle of the Bering-Bagley Glacier System from Observations and Numerical Modeling

Thomas Trantow¹ and Ute Herzfeld¹

¹University of Colorado, Boulder

November 22, 2022

Abstract

The recent surge of the Bering-Bagley Glacier System (BBGS), Alaska, in 2008-2013 provided a rare opportunity to study surging in a large and complex system. We simulate glacier evolution for a 20 year quiescent phase, where geometrical and hydrological changes lead to conditions favorable for surging, and the first two years of a surge phase where a surge-front propagates through the system activating the surging ice. For each phase, we analyze the simulated elevation-change and ice-velocity pattern, and infer information on the evolving basal drainage system through hydropotential analysis. During the quiescent phase simulation, several reservoir areas form at locations consistent with those observed. Up-glacier of these reservoir areas, water drainage paths become increasingly lateral and hydropotential wells form indicating an expanding storage capacity of subglacial water. These results are attributed to local bedrock topography characterized by large subglacial ridges that act to dam the down-glacier flow of ice and water. Based on the BBGS's end-of-quiescence state, we propose several surge initiation criteria to predict when the system is set to surge. In the surge simulation, we model surge evolution through Bering Glacier's trunk by implementing a new friction law that mimics a propagating surge-wave. Modeled surge velocities share spatial patterns and reach similar peaks as those observed in 2008-2010. As the surge progresses through the glacier, drainage efficiency further degrades in the active surging zone from its already inefficient, end-of-quiescence state. Satellite observations from 2013 indicate hydraulic drainage efficiency throughout the glacier was restored after the surge had ended.

1 **Evolution of a Surge Cycle of the Bering-Bagley**
2 **Glacier System from Observations and Numerical**
3 **Modeling**

4 **Thomas Trantow¹and Ute C. Herzfeld^{1,2}**

5 ¹Department of Electrical, Energy and Computer Engineering, University of Colorado, Boulder, Colorado,
6 USA

7 ²Cooperative Institute for Research in Environmental Sciences, University of Colorado, Boulder,
8 Colorado, USA

9 **Key Points:**

10

- 11 Using a full-Stokes approach and satellite observations, the dynamic, geometric
12 and hydraulic evolution of the BBGS during surge is modeled
- 13 Local bed topography controls the formation of reservoir areas, slows water drainage,
14 and retains water in trigger areas during quiescence
- 15 A new friction law for the surge phase is introduced based on observed proper-
ties of kinematic surge waves in the BBGS

16 **Abstract**

17 The recent surge of the Bering-Bagley Glacier System (BBGS), Alaska, in 2008-
 18 2013 provided a rare opportunity to study surging in a large and complex system. We
 19 simulate glacier evolution for a 20 year quiescent phase, where geometrical and hydro-
 20 logical changes lead to conditions favorable for surging, and the first two years of a surge
 21 phase where a surge-front propagates through the system activating the surging ice. For
 22 each phase, we analyze the simulated elevation-change and ice-velocity pattern, and in-
 23 fer information on the evolving basal drainage system through hydropotential analysis.
 24 During the quiescent phase simulation, several reservoir areas form at locations consis-
 25 tent with those observed. Up-glacier of these reservoir areas, water drainage paths be-
 26 come increasingly lateral and hydropotential wells form indicating an expanding stor-
 27 age capacity of subglacial water. These results are attributed to local bedrock topogra-
 28 phy characterized by large subglacial ridges that act to dam the down-glacier flow of ice
 29 and water. Based on the BBGS's end-of-quiescence state, we propose several surge ini-
 30 tiation criteria to predict when the system is set to surge. In the surge simulation, we
 31 model surge evolution through Bering Glacier's trunk by implementing a new friction
 32 law that mimics a propagating surge-wave. Modeled surge velocities share spatial pat-
 33 terns and reach similar peaks as those observed in 2008-2010. As the surge progresses
 34 through the glacier, drainage efficiency further degrades in the active surging zone from
 35 its already inefficient, end-of-quiescence state. Satellite observations from 2013 indicate
 36 hydraulic drainage efficiency throughout the glacier was restored after the surge had ended.

37 **Plain Language Summary**

38 The recent surge of the Bering-Bagley Glacier System (BBGS), Alaska, in 2008-
 39 2013 provided a rare opportunity to study surging in a large and complex system. A surge
 40 glacier cycles between a long period of normal flow and a short period of accelerated flow
 41 where large-scale deformations, such as crevasses, occur. We use a numerical model to
 42 simulate glacier evolution for both the quiescent phase and the initial surge phase of the
 43 BBGS. For each phase, we analyze the simulated elevation-change and ice-velocity, and
 44 infer information on the evolving hydraulic drainage system. During the quiescent phase
 45 simulation, mass build-ups form at locations consistent with those observed and water
 46 drainage paths become less efficient with expanding storage capacity of subglacial wa-
 47 ter. These results are attributed to local bedrock topography characterized by large sub-
 48 glacial ridges that act to dam the down-glacier flow of ice and water. In the surge sim-
 49 ulation, we model surge evolution through Bering Glacier by implementing a new fric-
 50 tion law that mimics a propagating surge-wave. As the surge progresses through the glacier,
 51 drainage efficiency further degrades in the areas of fast-moving ice. Satellite observations
 52 from 2013 indicate hydraulic drainage efficiency throughout the glacier was restored af-
 53 ter the surge had ended.

54 **1 Introduction**

55 The Bering-Bagley Glacier System (BBGS) in southeast Alaska stretches nearly
 56 200 km in length and covers an area greater than 5000 km² making it the largest tem-
 57 perate glacier system in the world (B. F. Molnia & Post, 2010) (see Figure 1). The BBGS
 58 is likely the largest surge glacier system outside of the major ice sheets with surge events
 59 occurring every 20-25 years (Post, 1972; B. F. Molnia & Post, 2010; Lingle et al., 1993;
 60 B. Molnia & Post, 1995; U. C. Herzfeld & Mayer, 1997; U. Herzfeld, 1998; B. Molnia &
 61 Williams, 2001; D. R. Fatland & Lingle, 1998; Mayer & Herzfeld, 2000; B. F. Molnia,
 62 2008; D. R. Fatland & Lingle, 2002; Roush et al., 2003; Fleischer et al., 2010; Josberger
 63 et al., 2010; R. A. Shuchman et al., 2010; R. Shuchman & Josberger, 2010). The most

64 recent surge of the BBGS in 2008-2013 (U. C. Herzfeld et al., 2013; Burgess et al., 2013)
 65 provides a rare opportunity to investigate surging in a large and complex glacier system.

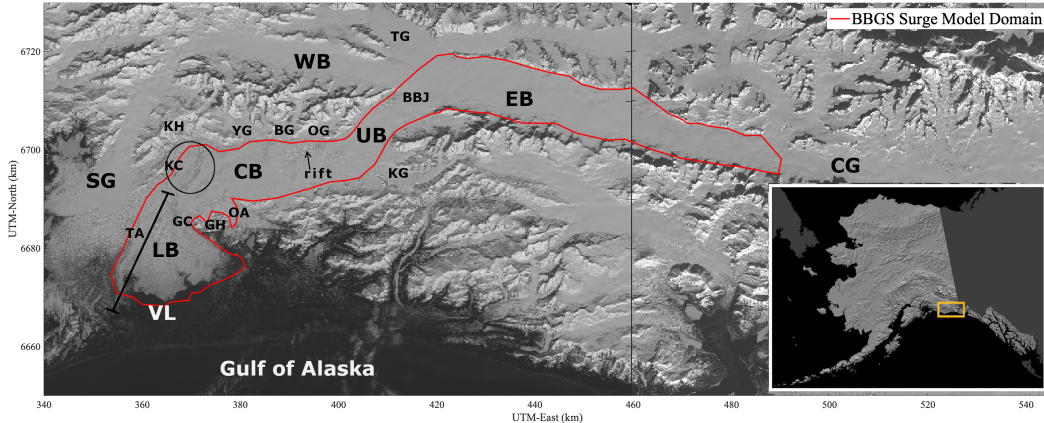


Figure 1. Key features in and around the Bering Bagley Glacier System including the numerical model domain. The red line marks the domain of the BBGS model. LB – Lower Bering Glacier, also referred to as the “lobe area” or the Bering Lobe, CB – Central Bering Glacier; UB – Upper Bering Glacier; EB – Eastern Bagley Ice Field; BBJ – Bering-Bagley Junction; WB – Western Bagley Ice Field; SG – Steller Glacier; CG – Columbus Glacier; VL – Vitus Lake; GH – Grindle Hills; GC – Grindle Corner; KH – Khitrov Hills; TG – Tana Glacier; YG – Yushin Glacier; BG – Betge Glacier; OG – Ovtsyn Glacier; KG – Kuleska Glacier; OA – Overflow Area also known as the Kaliakh Lobe; TA – Tashalish Arm (indicated by black line segment); KC – Khitrov Crevasses (circled in black). The rift is indicated by a black arrow in Upper Bering. The Eastern and the Western Bagley Ice Fields together are also referred to simply as the Bagley Ice Field (BIF). Note the combination of Upper and Central Bering Glacier constitute Bering Glacier’s “trunk” and the imaginary line connecting the Khitrov Hills to the Grindle Hills across Bering Glacier is referred to as Khitrov-Grindle Line. The BBGS is surrounded by the Chugach-Saint Elias mountain range. Background images from Landsat-8 acquired on 28 April 2013 (left) and 7 March 2014 (right). Reference image in lower right: U.S. Geological Survey Map I-2585.

1.1 Glacier Surging

67 A surge-type glacier cycles quasi-periodically between a long quiescent phase of reg-
 68 ular flow speeds and gradual retreat, and a short surge phase when ice flow accelerates
 69 10-100 times its normal velocity. During the quiescent phase, the geometry of a surge-
 70 type glacier changes by thickening in particular areas and thinning in others, resulting
 71 in regions of overall steepening often accompanied by observed “bulges” at the glacier
 72 surface (Meier & Post, 1969; Fowler, 1987; Raymond, 1988; U. C. Herzfeld & Mayer, 1997;
 73 U. Herzfeld, 1998; U. C. Herzfeld et al., 2013). This mass redistribution leads to defi-
 74 nitions of *reservoir areas*, defined as areas of general thickening during the quiescent phase,
 75 and *receiving areas* where mass is transferred during the surge phase.

76 An observed bulge often coincides with the surge “front” that propagates as a kine-
 77 matic wave down-glacier with resulting effects that propagate up-glacier as well. The down-
 78 glacier propagation is thought to change the basal hydrological conditions, perhaps through
 79 increased driving stress, leading to increased water pressure, reduced friction and thus
 80 increased basal motion (Fowler, 1987) that accounts for nearly all the observed dynam-

81 ics during a surge (Cuffey & Paterson, 2010). As the wave moves down-glacier, it acti-
 82 vates the increased basal motion for a section of the glacier (Fowler, 1987), leading to
 83 accelerating (surging) ice within this “activation zone”. The evolving bounds of the ac-
 84 tivation zone are given by a leading edge coinciding with the surge front and a trailing
 85 edge (Fowler, 1987). Studies on smaller surge-glaciers find that the entire glacier can be
 86 active at the same time once the activation-wave reaches the terminus, e.g. Finsterwalder-
 87 breen in Robin and Weertman (1973) whose length is ≈ 14 km. Turrin et al. (2013) maps
 88 the kinematic wave for the latest BBGS surge and suggest that the activated portion of
 89 the glacier extends up to the Bering-Bagley Junction (BBJ), near their proposed surge-
 90 trigger area.

91 Smaller-scale acceleration events are known to occur during the quiescent phase
 92 of some surge-glaciers leading to temporary relaxation of the increased driving force that
 93 accompanies surface steepening (Meier & Post, 1969; Raymond, 1987; Harrison & Post,
 94 2003). However, during the true surge phase, a rapid and full-scale acceleration event
 95 redistributes ice throughout the entire glacier system resulting in drastic elevation changes,
 96 with rapid thinning of the former reservoir areas, thickening in the receiving areas and
 97 drawdowns along the margins of the glacier (Meier & Post, 1969; Raymond, 1987; Har-
 98 rison & Post, 2003; Fowler, 1987, 1989). Heavy and wide-spread crevassing also occurs
 99 during the surge phase, indicative of rapid deformation, horizontal and vertical displace-
 100 ment of ice and sudden changes in flow speeds.

101 Most studies on surges are conducted on smaller glaciers that consist of a single
 102 reservoir area in the accumulation zone and a single reservoir area down-glacier near the
 103 terminus, e.g., Variegated Glacier, Alaska (W. Kamb et al., 1985; Eisen et al., 2005; Jay-
 104 Allemand et al., 2011a) or Black Rapids Glacier, Alaska (Raymond et al., 1995; Hein-
 105 richs et al., 1996; D. Fatland et al., 2003). However, as we show in this study, a large and
 106 complex glacier system like the BBGS can consist of multiple reservoir and receiving ar-
 107 eas which can lead to a complicated picture of the surge evolution. Moreover, a complex
 108 glacier system can have both surge-type and non-surge-type parts, with different pro-
 109 cesses, such as surge initiation and re-initiation, occurring in different locations and at
 110 different times (U. Herzfeld, 1998; U. C. Herzfeld et al., 2013). The BBGS shares this
 111 property of complexity with sections of the Greenland and Antarctic ice sheet margins,
 112 where surge-type glaciers are found neighboring non-surge-type glaciers and accelerat-
 113 ing outlet glaciers (Jiskoot, 1999; U. C. Herzfeld, 2004; Sevestre et al., 2015). Thus, the
 114 study of the BBGS surge provides extra layers of insight into the complex glacier accel-
 115 eration found along the ice sheet margins, compared to the more commonly studied surges
 116 of smaller mountain glaciers.

117 In general, surge-type glaciers are present in distinct climatic environments and tend
 118 to have greater areas, longer lengths and lower surface gradients than non-surge-type glaciers
 119 (Sevestre et al., 2015; Benn et al., 2019). While internal dynamics are believed to gov-
 120 ern glacial surging, climatic effects, including mass balance and even weather, are known
 121 to effect surge initiation, termination, and the length of each phase in the surge-cycle
 122 for some glaciers (Harrison & Post, 2003). Murray et al. (2003) point out there may not
 123 be a single surge mechanism due to observed differences between surge glaciers found
 124 in Alaska and those found in Svalbard. Svalbard, or Arctic, glacier systems contain poly-
 125 thermal ice while glaciers in southeast Alaska comprise entirely of temperate ice, that
 126 is, ice at or near the melting point. The BBGS is an ideal prototype of the Alaskan-type
 127 surge. During the summer in southeast Alaska, warmer temperatures induce surface melt-
 128 ing throughout the glacier system. The meltwater is transferred to the base through englacial
 129 tunnels, or moulin, thus requiring the formation of drainage system at the ice/bedrock
 130 interface to transfer the water down-glacier.

131 Alaskan-type surges are associated with rapid changes in the subglacial hydraulic
 132 drainage system (W. Kamb et al., 1985). The system may consist of flow through chan-
 133 nels or linked-cavities in the basal ice or bedrock (hard-bed case), or through a deformable

134 sediment (or till) layer at the ice-bed interface (soft-bed case) (Weertman, 1972; Lliboutry,
 135 1968; Shoemaker, 1986; W. B. Kamb, 1987; Fowler, 1987; Murray, 1997; Björnsson, 1998;
 136 Truffer et al., 2000). In the case of a hard bed, sliding of the ice over the rigid bedrock
 137 constitutes the dominant process of rapid glacier flow while the soft-bed case implies de-
 138 formation of a subglacial till layer. Observations of basal morphologies indicate most Alaskan
 139 glaciers have an underlying till layer (Harrison & Post, 2003). While the exact physics
 140 relating to surge initiation and motion are different between the two cases, a reduction
 141 in the hydraulic drainage efficiency would result in increased basal water pressures and
 142 increased basal sliding speeds in both cases (Harrison & Post, 2003). In the current study,
 143 we do not distinguish the bed-type, and instead focus on water pressure and drainage
 144 efficiency inferred from hydropotential calculated at the ice-bed boundary and its rela-
 145 tion to basal motion via a friction law.

146 A surge is accompanied by a rapid switch from a generally efficient drainage sys-
 147 tem (EDS), characterized by low-subglacial water pressures, to an inefficient drainage
 148 system (IDS) with high basal water pressures (W. Kamb et al., 1985; Harrison & Post,
 149 2003). At any given time, a surge-type glacier can be a tightly-coupled combination of
 150 both an EDS and an IDS (Björnsson, 1974; Shoemaker & Leung, 1987; Björnsson, 1998;
 151 Boulton et al., 2007; Magnússon et al., 2010). During quiescence however, the glacier sys-
 152 tem is almost entirely comprised of an EDS. A secularly evolving glacier geometry over
 153 the course of quiescence leads to conditions that initiate a surge through destruction of
 154 the EDS with a transition to a persistent IDS during the surge phase (W. B. Kamb, 1987;
 155 Harrison & Post, 2003). A key difference between the two systems is how they react to
 156 an increase in water discharge to the base. In this case, basal water pressures increase
 157 throughout an IDS whereas an EDS will increase its capacity to store the increased dis-
 158 charge leading to lower pressures (de Fleurian et al., 2018). A hydraulic system must be
 159 able to maintain high water pressures for some time in order for the IDS to persist and
 160 grow thus initiating a full-scale surge (W. B. Kamb, 1987).

161 Subglacial and englacial water storage contribute to the switching and persistence
 162 of hydraulic regimes (Harrison & Post, 2003). The destruction of an EDS traps water
 163 that would have normally drained allowing the rapid increase of basal water pressure as-
 164 sociated with an IDS. The persistence of an IDS, and its expansion to more parts of the
 165 glacier system, depends on the amount of stored water available to maintain high basal
 166 water pressures. In this paper, we show that over the course of quiescence, Bering Glacier
 167 evolves the capacity to store more and more englacial and subglacial water through the
 168 development of hydropotential wells and longer, more-transverse drainage paths, thus
 169 complicating the concept of an EDS as described above. We also investigate the progres-
 170 sion of the surge as it relates to an expanding IDS, maintained by exacerbated drainage
 171 inefficiencies.

172 Finally, stored water during a surge is reflected by the occurrence of large outburst
 173 floods at the glacier terminus, which is accompanied by surge termination and a return
 174 to normal flow, lower water pressures and an EDS (Humphrey & Raymond, 1994; Har-
 175 rison & Post, 2003). Such outburst floods have been observed for previous surges of the
 176 BBGS (D. R. Fatland & Lingle, 1998). The current study uses CryoSat-2 elevation data
 177 to demonstrate that after a surge of the BBGS, the glacier drainage reverts to a more
 178 efficient drainage system with less capacity to store subglacial and englacial water.

179 1.2 Observations of the Recent BBGS Surge

180 The onset of the latest major surge event in Bering Glacier occurred in early 2011
 181 affecting mostly Lower and Central Bering Glacier (Figure 2) (U. C. Herzfeld et al., 2013),
 182 while lesser surge activity was observed near in Upper Bering Glacier after the opening
 183 of a giant longitudinal rift (Figure 2(a-b)) where elevated ice-velocities were observed in
 184 2008 (U. C. Herzfeld et al., 2013; Burgess et al., 2013). This rift, also observed during

185 the 1993-1995 surge (U. Herzfeld, 1998), reached 60 m in depth upon forming and grew
 186 in size throughout the surge reaching nearly 200 m in width and 10 km in length by 2013
 187 (U. C. Herzfeld et al., 2013; Trantow, 2020).

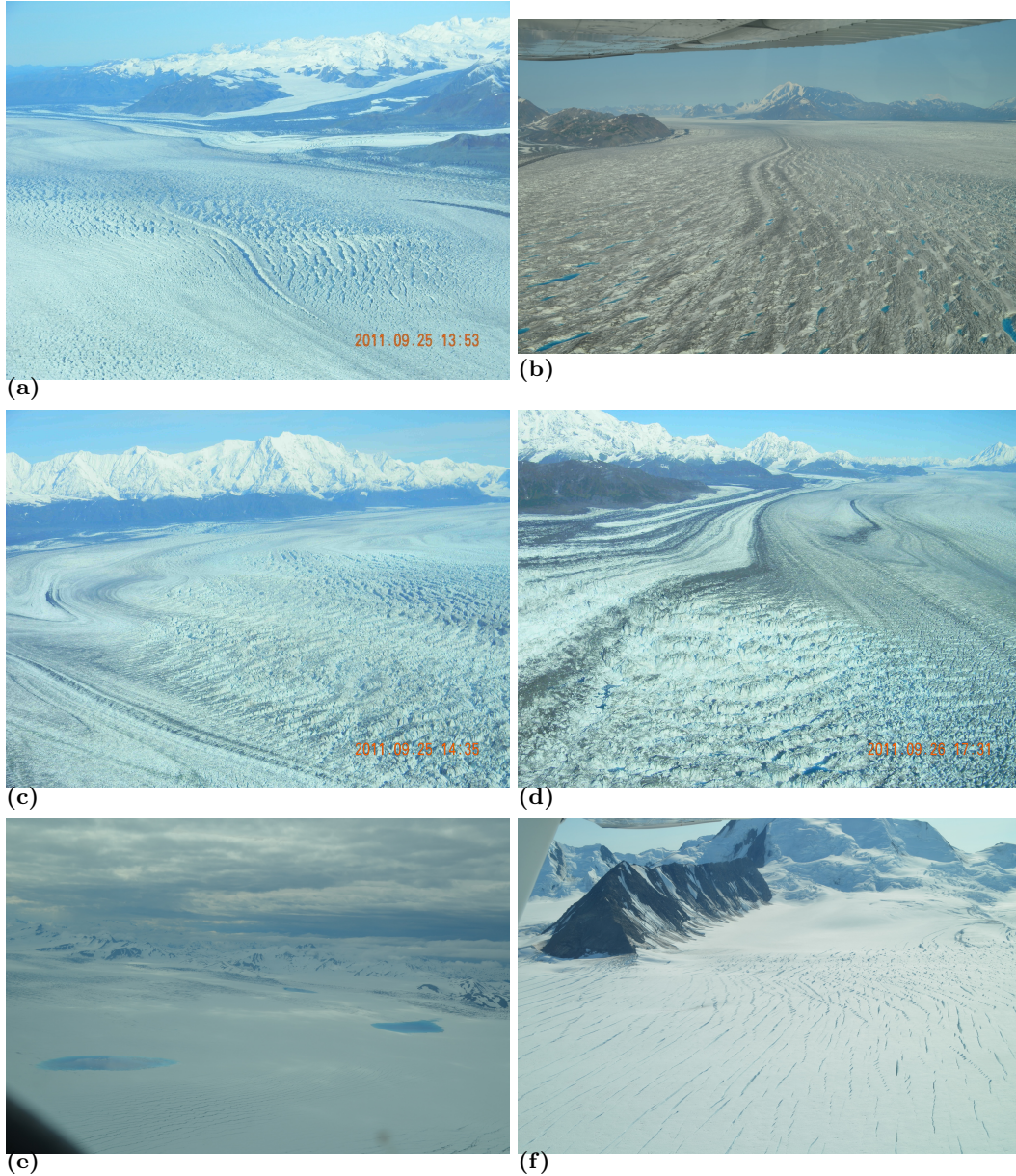


Figure 2. Imagery from the airborne campaign flights over Bering Glacier 2011-2013. (a) Large longitudinal rift in Upper Bering Glacier along the northern branch in September 2011(looking down-glacier) and (b) in August 2013 with water in the surrounding crevasse field (looking up-glacier), (c) upper Tashalish Arm (September 2011), (d) Khitrov Crevasses (foreground) formed during the second stage of the surge in early-2011 (September 2011), (e) three supraglacial lakes in Central Bering Glacier as observed in July 2012, and (f) en-échelon crevasses along the southern margin of the upper Bagley Ice Field (August 2013).

188 Surface speeds in late 2007 and early 2008 were around 1 m/day (365 m/a) in the
 189 Bagley Ice Field and Upper-Bering Glacier (LeBlanc, 2009). Between September 2008

190 and February 2009 the BBGS accelerated progressively from the BBJ to the lower-mid
 191 glacier right above the overflow area (Turrin et al., 2013; Burgess et al., 2013). The max-
 192 imum recorded velocity was 7 m/day (2555 m/a) near mid-glacier but peak speeds might
 193 have been even higher (Burgess et al., 2013). In early 2010, surface speeds in Lower and
 194 Central Bering Glacier returned close to normal quiescent speeds and velocities in the
 195 lower Bagley Ice Field and Upper Bering were measured at around 2 m/d (720 m/a).

196 In early 2011, Bering Glacier's dynamics changed to a full-scale surge resulting in
 197 crevassing throughout a large portion of the glacier (U. C. Herzfeld et al., 2013). The
 198 recently heightened reservoir area, i.e. a bulge, in the lower-central Bering, observed by
 199 (U. C. Herzfeld et al., 2013) and (Burgess et al., 2013), transferred its mass down-glacier
 200 along the northern branch of the flow regime to the lower Tashalish arm area (the west-
 201 ernmost part of the Bering lobe, Figure 2(c)). The former reservoir area experienced sur-
 202 face lowering of 40-70 meters while the receiving area gained 20-40 meters of surface el-
 203 evation by fall 2011 (U. C. Herzfeld et al., 2013). The bulge collapse resulted in the for-
 204 mation of large surge crevasses in the Khitrov crevasse field (Figure 2(d)). The thick-
 205 ening continued to move downstream until it reached the terminus, where it extended
 206 2-4 km (Turrin et al., 2013).

207 There were very few measurements of velocity during 2011 provided by Burgess et
 208 al. (2013), but one 11 day interval in the beginning of July showed a peak velocity of 9
 209 m/day (3285 m/a) near the boundary of Upper and Central Bering Glacier. Burgess et
 210 al. (2013) provided no velocity measurements in the Lowerf Bering Glacier. Velocity mea-
 211 surements of Lower Bering from Trantow and Herzfeld (2018) revealed that surge veloc-
 212 ities in early 2011 reached at least 21 m/day.

213 Aerial observations from the campaigns of U. C. Herzfeld et al. (2013) revealed that
 214 the surge continued to induce significant effects throughout the glacier system in 2012
 215 and 2013. The presence of large supraglacial lakes in the summer of 2012 in Central Bering
 216 (Figure 2(e)) indicated that the glacier remained in a state of inefficient drainage. By
 217 2013 most of the dynamical activity in Bering Glacier had ceased though the effects of
 218 the surge were still being felt in the Bagley Ice Field as demonstrated by the opening
 219 of fresh en-échelon crevasses (Figure 2(f)). These characteristic en-échelon crevasses form
 220 when the kinematic energy from the surge causes deformation at pre-existing weaknesses
 221 in the ice (crevasses) caused by the local topography (U. C. Herzfeld & Mayer, 1997).
 222 A more comprehensive documentation of observations from latest surge is given in Chap-
 223 ter 2 of Trantow (2020).

224 While it is not simple and obvious to assign the time of surge initiation and surge
 225 termination in a complex glacier system like the BBGS, for the purposes of this study
 226 we presuppose that the most recent surge initiated in early-2008 in Upper Bering near
 227 the rift area. The surge from 2008-2010 constitutes the first, or initial surge phase. We
 228 then refer to the surge activity in 2011-2013 as the second, or major, surge phase as most
 229 of the dynamical activity occurred during this time (U. C. Herzfeld et al., 2013).

230 2 Approach

231 In this study we conduct prognostic simulations using the model introduced in Trantow
 232 and Herzfeld (2018) to investigate changes that occur in the BBGS during a quiescent
 233 and early-surge phase. For each phase, we analyze mass redistribution within the glacier
 234 system to help estimate changes in hydrological drainage characteristics, which are known
 235 to play a major role in flow behavior and state switching in a surge-type glacier. The
 236 most important aspect of our ice-flow model is the treatment of the ice-bed boundary,
 237 that is, the input bedrock topography and the prescribed friction law (Section 3.2.2). While
 238 the input bedrock topography remains fixed throughout the surge cycle, parameters of

239 the basal friction law are different for each phase and will spatiotemporally evolve dur-
 240 ing the surge phase reflecting a passing surge-wave (Section 3.2.2.2).

241 The BBGS model was built using the finite element software Elmer/Ice (Gagliardini
 242 et al., 2013) and has been used in previous diagnostic studies that used a crevasse-based
 243 approach to constrain unknown model parameters during the early-2011 phase of the lat-
 244 est BBGS surge (Trantow & Herzfeld, 2018). Our previous work focused on synthesiz-
 245 ing the model-data connection using a variety high-quality data inputs, which includes
 246 observations of surface height (Trantow & Herzfeld, 2016), velocity, crevasse location and
 247 crevasse orientation (Trantow & Herzfeld, 2018), and showed that model results and pa-
 248 rameter optimization were robust to relative uncertainties in the observational inputs
 249 (Trantow et al., 2020). In the current study, we switch to prognostic modeling by per-
 250 forming longer transient simulations while using the same optimized model parameter-
 251 ization and high quality observational data sets derived in our previous studies.

252 With relatively high resolution bedrock and ice-surface topography inputs, our ap-
 253 proach for modeling basal friction during quiescence and the surge phase allows glacier
 254 geometry to explain as much of the spatial variability in the glacier's dynamics as pos-
 255 sible. That is, we do not fit friction parameters based on observed velocity, e.g. (Larour
 256 et al., 2014), and instead attempt to keep parameterization as simple as possible in or-
 257 der to adequately capture observed dynamic behavior. Discrepancies in modeled and ob-
 258 served behaviors informs the next step up in complexity with regards to the basal fric-
 259 tion law in both the quiescent and surge phases (Section 4.4).

260 Our modeling approach here does not include seasonal variability but instead looks
 261 at inter-annual (secular) trends. For example, we enforce an observed mean annual sur-
 262 face mass balance (SMB) uniformly throughout the entire model duration. While sea-
 263 sonal changes in glacial water are known to play a role in the intra-annual timing of surges
 264 (Raymond, 1987), our analysis will focus on inter-annual and seasonally-independent changes
 265 in hydrological characteristics of the subglacial drainage system, which govern the ap-
 266 proximate length of the surge cycle phases. That is, we focus on modeling dynamics re-
 267 sulting from internal characteristics of the glacier system, which are known to determine
 268 whether a glacier is or is not a surge-type glacier. If surging depended strongly on sea-
 269 sonal components such as precipitation, then we would expect neighboring glaciers to
 270 have similar dynamic responses as those observed for the BBGS. For example, neighbor-
 271 ing Steller Glacier (see Figure 1) is not known to surge. In fact, Trantow (2020) has shown
 272 that local precipitation and temperature anomalies have no correlation with the timing
 273 and duration of the last three BBGS surges.

274 In part due to computational limitations at the time of analysis, we simulate the
 275 quiescent phase and initial surge phase of the BBGS cycle separately. We use observed
 276 geometry in 2016, when the BBGS is in a fully quiescent state, to initialize the 20 year
 277 quiescent simulation. The end-of-quiescence geometry is then used to initialize the 2-year
 278 early-surge phase simulation. While the two phases are simulated separately, the geo-
 279 metric and hydrologic characteristics of the BBGS at the end of quiescence inform pro-
 280 posals for surge initiation criteria that may be used in future simulations that aim to sim-
 281 ulate the entire BBGS surge cycle in a single run. Due to the computational resources
 282 required to simulate the entire surge phase using the full-Stokes representation, we rely
 283 on satellite observations to interpret the second surge phase that last occurred in 2011-
 284 2013 rather than explicit modeling.

285 Our successful model simulations provide valuable insight into the surge of the BBGS,
 286 which we cover in this paper. After introducing the salient model aspects in Section 3,
 287 we analyze the simulation of results of the quiescent phase in Section 4 and the early-
 288 surge phase in Section 5. For each phase, we investigate (1) the mass redistribution and
 289 geometrical changes in the glacier system, (2) the hydrological implications of those changes,
 290 and (3) how these results can improve our model representations. Observations of sur-

291 face height, velocity and mass balance help guide and validate our modeling efforts through-
 292 out. In addition, we propose methods for initiating a surge in Section 5.1 while in Sec-
 293 tions 5.3 and 5.4 we use velocity maps and CryoSat-2 observations from the end of the
 294 latest surge in 2013 to investigate the state of the glacier system at the end of the surge
 295 phase.

296 3 Numerical Model

297 For numerical experiments of ice flow and crevassing, we have created a 3D finite
 298 element model of the BBGS using the open-sourced software Elmer/Ice (Gagliardini et
 299 al., 2013). The BBGS model is covered in depth in Trantow and Herzfeld (2018) in re-
 300 lation to diagnostic surge experiments and model-data connection. In the current sec-
 301 tion, we cover only the salient model details and introduce several new aspects required
 302 for the longer prognostic simulations performed for this paper.

303 3.1 Flow Law for Temperate Ice

304 As mentioned previously, we employ the full-Stokes representation to model the com-
 305 plex glacier dynamics of the surging BBGS. The full-Stokes equations utilize conserva-
 306 tion laws to describe the flow of ice via internal deformation as forced by gravity. They
 307 have no simplifying assumptions on the stress regime, in contrast to the common Shal-
 308 low Ice (SIA) or Shallow Shelf (SSA) approximations. Stokes flow simplifies the more
 309 general Navier-Stokes equations for viscous fluid flow by assuming the inertial forces are
 310 negligible in comparison to viscous forces. Momentum conservation is given by

$$311 \nabla \cdot \boldsymbol{\sigma} + \rho \mathbf{g} = \nabla \cdot (\boldsymbol{\tau} - p \mathbf{I}) + \rho \mathbf{g} = 0, \quad (1)$$

312 and conservation of mass is given by

$$313 \nabla \cdot \mathbf{u} = \text{tr}(\dot{\boldsymbol{\epsilon}}) = 0, \quad (2)$$

314 where $\boldsymbol{\sigma} = \boldsymbol{\tau} - p \mathbf{I}$ is the Cauchy stress tensor, $\boldsymbol{\tau}$ the deviatoric stress tensor, p the pres-
 315 sure, ρ the ice density, $\mathbf{g} = (0, 0, -9.81)$ the gravity vector, \mathbf{u} the velocity vector and
 316 $\dot{\boldsymbol{\epsilon}} = \frac{1}{2}(\nabla \mathbf{u} + (\nabla \mathbf{u})^T)$ the strain-rate tensor.

317 The relation between stress and the internal flow of ice is given by Glen's Flow Law,

$$318 \boldsymbol{\tau} = 2\eta \dot{\boldsymbol{\epsilon}}, \quad (3)$$

319 where η is the effective viscosity defined as,

$$320 \eta = \frac{1}{2} A^{-1/n} \dot{\epsilon}_e^{(1-n)/n}, \quad (4)$$

321 where $\dot{\epsilon}_e$ is the effective strain-rate and n the Glen exponent, set as $n = 3$ for all ex-
 322 periments in this study, which is a well established value for temperate glacier flow (Greve
 323 & Blatter, 2009; Cuffey & Paterson, 2010). The rate-factor $A = A(T')$ is a rheologi-
 324 cal parameter, which depends on the ice temperature via an Arrhenius law, is given by

$$325 A(T') = A_0 \exp\left(\frac{-Q}{RT}\right), \quad (5)$$

326 where Q is the activation energy, R the universal gas constant, A_0 a pre-exponential con-
 327 stant, and T' the temperature relative to the pressure melting point. The BBGS is a tem-
 328 perate glacier, implying the temperature of most of the ice is at or near the pressure melt-
 329 ing point throughout the entire year. Therefore, we employ an isothermal assumption
 330 with ice temperature set to 0°C resulting in a rate-factor of $A(0^{\circ}\text{C}) = 75.7 \text{ MPa}^{-3} \text{ a}^{-1}$.

331 3.2 Boundary Conditions

332 3.2.1 Ice/Atmosphere Boundary

333 At the surface of the glacier, a stress-free boundary condition is employed

$$334 \quad \boldsymbol{\sigma} \mathbf{n}_s = -p_{atm} \boldsymbol{\sigma} \approx 0 \quad (6)$$

335 which assumes the atmospheric pressure, p_{atm} , acting as a stress normal to the ice sur-
 336 face, $\boldsymbol{\sigma} \mathbf{n}_s$, is negligible with regards to its effect on ice flow. We also allow our glacier
 337 surface to freely evolve in order to investigate elevation change. The upper free surface
 338 is governed by an advection equation

$$339 \quad \frac{\partial z_s}{\partial t} + u_s \frac{\partial z_s}{\partial x} + v_s \frac{\partial z_s}{\partial y} - w_s = a_s, \quad (7)$$

340 where $\mathbf{u}_s = (u_s, v_s, w_s)$ is the surface velocity vector given by the Stokes equation (Equa-
 341 tion 2) and a_s is the accumulation or ablation component prescribed in the direction nor-
 342 mal to the surface (Gagliardini et al., 2013). The accumulation and ablation term we
 343 apply in our BBGS simulations is given by observations of mean surface mass balance
 344 with respect to elevation from Tangborn (2013) from 1951 to 2011 and from surface mass
 345 balance (SMB) observations of Alaskan glaciers from Larsen et al. (2015) (see Section
 346 3.4).

347 Initial ice-surface topography for the quiescent phase is derived from CryoSat-2 data
 348 using waveform analysis that combines a swath-processing technique together with the
 349 Threshold First Maximum Retracking Algorithm (TFMRA) (Helm et al., 2014). A specif-
 350 ically designed filter is applied to eliminate outliers in the dataset before utilizing the
 351 Advanced Kriging method (a form of Ordinary Kriging) to derive a 200 m resolution Dig-
 352 ital Elevation Model (DEM) of the entire BBGS surface (Trantow & Herzfeld, 2016). The
 353 influence of CryoSat-2 data processing techniques on elevation analysis and numerical
 354 modeling results is given in Trantow et al. (2020).

355 Quiescent experiments presented in this paper are initialized using a DEM derived
 356 from aggregated CryoSat-2 TFMRA-swath data from May 2016 to October 2016 (Sum-
 357 mer 2016), which corresponds to the initial quiescent phase geometry after the most re-
 358 cent surge. Initial topography for the surge phase experiments are given by the final state
 359 of the quiescent simulation. Note that for all experiments in this paper, the FEM grid-
 360 resolution is set to 400 m element lengths, which is identical to the resolution for sim-
 361 ulations in Trantow and Herzfeld (2018).

362 3.2.2 Ice/Bed Boundary

363 The ice-bed boundary condition specifies a friction, or sliding, law that specifies
 364 the relationship between basal shear stress and basal velocities and is an important as-
 365 pect of modeling surge behavior (B. Kamb, 1970; Clarke et al., 1984; W. B. Kamb, 1987).
 366 In this section, we cover the both the linear friction law used in modeling the quiescent
 367 phase and spatiotemporally evolving law for the surge phase. The surge-phase friction
 368 law is an extension of the linear friction law and is modeled to represent the evolution

369 of a surge wave, or “surge-front”, that propagates down-glacier during the surge along
 370 the central flowline of the glacier.

371 As mentioned previously, we do not consider bed composition in our simulations
 372 (hard vs. soft bed representation) and instead simply model the effect of changing fric-
 373 tion at the ice-bed interface. Following Harrison and Post (2003), we use the term “basal
 374 motion” to represent the various processes under the ice that result in non-zero basal
 375 velocities. Basal motion accounts for nearly all the dynamics during a surge with in-
 376 ternal deformation contributing very little to the observed ice-velocities (Cuffey & Pa-
 377 terson, 2010). Even in the quiescent phase of the BBGS, significant basal motion is re-
 378 quired to capture the observed velocities throughout most of quiescence (Trantow, 2020).

379 We estimate the unknown basal friction law parameters through model-data com-
 380 parisons of crevasses and surface velocities as described for the early-2011 surge phase
 381 in (Trantow & Herzfeld, 2018) and for the quiescent phase in (Trantow, 2020). By es-
 382 timating these parameters using observations, we essentially bypass the need to explic-
 383 itly model the basal water pressure responsible for the changing basal motion. Some fric-
 384 tion laws allow one to infer the basal water pressure after estimating the unknown pa-
 385 rameters (see Jay-Allemand et al. (2011b)). A lack of hydrological observations for the
 386 BBGS makes these inferences difficult, however we attempt to describe basal conditions
 387 in relation to water storage and drainage efficiency based on the modeled mass redistri-
 388 bution and inferred hydropotential (see Section 3.3).

389 We begin by introducing aspects common to both basal friction representations.
 390 For each, we assume ice flow does not penetrate the basal boundary, that is, there is no
 391 normal component to ice velocity at the base

$$392 \quad \mathbf{u} \cdot \mathbf{n}_b = 0 \quad (8)$$

393 where \mathbf{n}_b is the unit surface normal vector pointing outward to the bedrock surface (Gagliardini
 394 et al., 2013).

395 The input basal bedrock topography, common to all our BBGS simulations, is de-
 396 rived from ice-penetrating radar measurements provided by the Warm-Ice Sounding Ex-
 397 plorer (WISE) acquired during a 2012 campaign to the BBGS by NASA’s Jet Propul-
 398 sion Laboratory (Rignot et al., 2013). Derivation of bedrock topography DEMs of the
 399 BBGS is described in Trantow and Herzfeld (2018) and in Chapter 4.1 of Trantow (2020).

400 3.2.2.1 Linear Friction Law for the Quiescent Phase

401 Basal motion in the direction tangent to the basal surface normal takes place through-
 402 out the entire BBGS system during most of the surge cycle, aside from a short (~ 1 year)
 403 time period immediately after the surge ceases and basal water pressures are fully re-
 404 lieved, when observed ice velocities in Lower and Central Bering Glacier can be fully cap-
 405 tured using a no-slip boundary condition (Trantow, 2020). Experimentation in Trantow
 406 (2020) and Trantow (2014) show mean basal motion during quiescent flow, throughout
 407 the entire glacier system, is approximated using a linear sliding law

$$408 \quad \sigma_{nti} = \beta u_{ti}, \quad \text{for } i = 1, 2, \quad (9)$$

409 which relates the basal shear stresses, σ_{nti} , to the basal velocities, u_{ti} , through the lin-
 410 ear friction coefficient β . A constant and uniform value of $\beta = 10^{-4} \frac{\text{MPa}\cdot\text{a}}{\text{m}}$ is used for
 411 quiescent flow as informed by velocity observations during quiescence (Trantow, 2014,
 412 2020). The uniform prescription of β across the entire glacier system serves as a first-
 413 order approximation of the basal conditions during quiescence. We expect the friction

414 coefficient to depend on effective pressure, $\beta = \beta(N)$, which would not be uniform through-
 415 out the glacier. While the results of our first-order quiescent simulation match observa-
 416 tions quite well, we suggest ways to improve the spatiotemporal distribution of β based
 417 on model results and observed quiescent velocities in Section 4.4.

418 **3.2.2.2 Spatiotemporal Friction Law for the Surge Phase**

419 During a surge, the linear friction representation adequately captures the spatiotem-
 420 porally local behaviors of ice flow as shown in (Trantow & Herzfeld, 2018). That is, the
 421 linear sliding law accurately captures observed ice dynamics for an ~ 20 km longitudi-
 422 nal segment of the glacier for ~ 3 months. This spatiotemporal-segment of ice dynam-
 423 ics corresponds to the ice that is actively surging during the surge-phase evolution. We
 424 use this information, along with additional velocity observations, to derive a spatiotem-
 425 porally evolving basal friction law for the surge phase that utilizes the linear relation-
 426 ship between basal shear stress and basal velocities. This amounts to finding a distri-
 427 bution for the linear friction coefficient that evolves in space and time, $\beta = \beta(x, t)$. Phys-
 428 ically, the law models the propagation of a surge front, which acts as an activation-wave
 429 that changes basal conditions, a la (Fowler, 1987). We use observations of a propagat-
 430 ing front prior to and during the latest BBGS surge in 2008-2013 to estimate parame-
 431 ters in the new spatiotemporally-varying friction law that follows (Turrin et al., 2013;
 432 Trantow, 2020).

433 These parameters include the surge-wave propagation speed, u_{sf} , the surge-wave
 434 initiation location x_{init} , a minimum linear friction coefficient, β_{min} , corresponding to the
 435 peak surge velocity, and a linear friction coefficient corresponding to unactivated ice, β_q ,
 436 equivalent to the quiescent phase value. These parameters help define a spatial distri-
 437 bution of basal linear friction values that evolves in time throughout the surge phase.
 438 The surge-phase friction law is specified along a 1D central flowline, whose distance from
 439 the upper glacier boundary is given by x (see Figure 3). Values for β throughout the 2D
 440 ice-bed interface are given by the closest along-flowline point. A more complex repre-
 441 sentation is needed to capture the transverse variations in glacier flow that have been
 442 observed in Central Bering Glacier during a surge, which manifest as branches in the flow
 443 regime divided by the deep central glacier trough (U. C. Herzfeld et al., 2013; Trantow,
 444 2020).

445 A formula for the propagation speed of the surge front, u_{sf} , is given by Fowler (1987)
 446 in terms of heights and velocities for each edge of the surge front. In our implemen-
 447 tation of the surge wave here however, we assign a fixed propagation speed of 50 m/day
 448 which is on par with the observed propagation speed of the kinematic wave from 2008-
 449 2010 through Bering's trunk an into the lobe area (Turrin et al., 2013). Characteristics
 450 of the glacier at the end of quiescence will inform a choice of a surge initiation location
 451 along-flowline x_{init} (see Section 5.1).

452 With the surge-wave propagation speed and the initiation location we can define
 453 the bounds an activation zone of actively surging ice, given by the leading and trailing
 454 edge locations, at any time during the surge phase: $x_{active}(t) = x \in [x_{trail}(t), x_{lead}(t)]$.
 455 The location of the leading edge of the surge front is given by:

$$456 \quad x_{lead} = x_{init} + u_{sf} \cdot t \quad (10)$$

457 where t is simulation time in years. Based on velocity observations of the surge front prop-
 458 agation in Turrin et al. (2013), we set the trailing edge location equal to the initiation
 459 location since velocities appear to be elevated in Upper Bering Glacier throughout the
 460 surge in 2008 through 2010. Therefore,

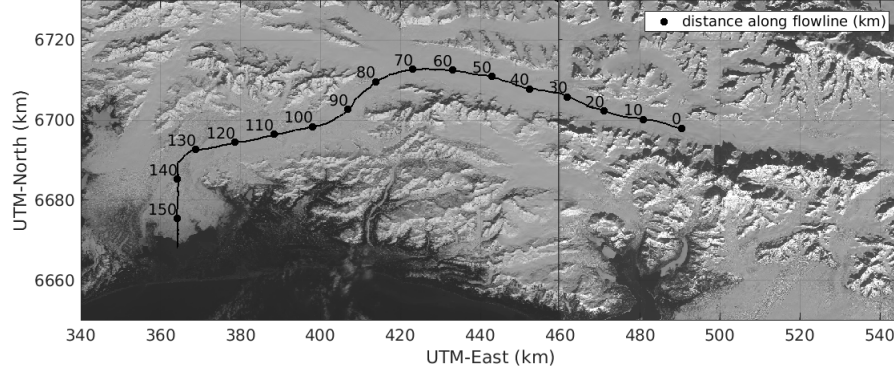


Figure 3. Flowline along the BBGS with 0 km corresponding to the uppermost point the system in the Bagley Ice Field. The Bagley Ice Field stretches from km-0 to the Bering-Bagley Junction (BBJ) at km-80. Upper Bering roughly corresponds to segment of Bering Glacier from km-80 to km-100, Central Bering from km-100 to km-130 and Lower Bering (or the Bering Lobe) from km-130 to km-155 at the terminus. Most of the interesting surge dynamics occur in Bering's main “trunk” which stretches from km-80 to km-135.

461

$$x_{trail} = x_{init} \quad (11)$$

462
463

Ice up-glacier and down-glacier of the activation zone is considered “unactivated ice” and is assigned the quiescent phase value for the linear friction coefficient, β_q .

464
465
466
467
468
469
470
471
472
473
474
475
476
477
478
479

The final part of defining of basal friction coefficient during the surge-phase is given by the distribution of the β values within the activation zone. Observed surface speeds are largest near the leading edge and generally decrease as you move up-glacier (W. Kamb et al., 1985; Fowler, 1987; Raymond et al., 1987). By estimating linear friction values from observed surface velocity data from the 1982-1983 surge of Variegated Glacier, Jay-Allemand et al. (2011b) found the β distribution within the activation zone resembled a normal curve whose peak was near the leading edge. At some times during the surge, the estimated β distribution contained an additional peak up-glacier of the leading edge, which Raymond et al. (1987) suggest is due to irregularities in the bedrock topography. Based on the distribution of model-data discrepancy in surge velocities in lower Bering in Trantow and Herzfeld (2018), we decide to use a simple linear distribution of β within the activation zone. We assign the minimum friction coefficient at the leading edge of the surge front, β_{min} , and have β linearly increase throughout the activation zone until its end at the trailing edge where the friction coefficient is set to its quiescent value, β_q . Given the description here, the linear friction coefficient along the entire flowline axis (x) is defined mathematically as:

480
481
482

$$\beta(x, t) = \begin{cases} \beta_{min} + (\beta_q - \beta_{min}) \frac{x_{lead}(t) - x}{x_{lead}(t) - x_{trail}}, & \text{if } x_{trail} \leq x \leq x_{lead} \\ \beta_q, & \text{otherwise} \end{cases} \quad (12)$$

483
484

for $t > 0$, with $t = 0$ corresponding to the time of surge initiation. The simulations in this paper use a quiescent friction coefficient of $\beta_q = 10^{-4} \frac{MPa \cdot a}{m}$ based on results

485 from Trantow (2014). The surge-front basal friction coefficient value, β_{min} , is set to $\beta_{min} =$
 486 $10^{-5} \frac{MPa \cdot a}{m}$, which comes from a result of optimizing the linear basal friction coefficient
 487 for the surge front in early-2011 (Trantow & Herzfeld, 2018). The linear transition be-
 488 tween the two values within the activation zone describes an approximation to the ob-
 489 served surge progression during the latest surge, as mentioned previously. A diagram of
 490 the basal friction coefficient distribution within the activation zone is given in Figure 4.

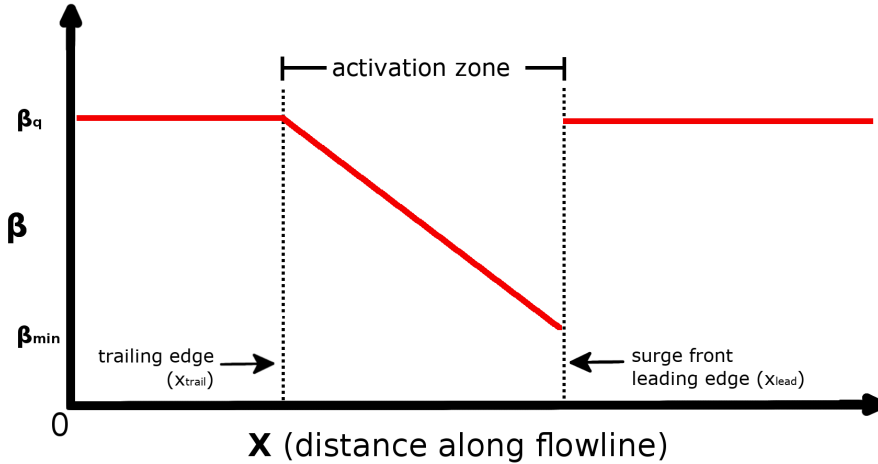


Figure 4. Linear basal friction coefficient distribution during the surge phase.

Basal friction coefficient, β , versus along-flowline distance, x , where $x = 0$ is the uppermost location in the Bagley Ice Field.

491 3.2.3 Lateral Boundary

492 The material similarity of the glacier's base and margins leads to a prescription of
 493 the linear friction law at the lateral boundary as well. However, the friction coefficient
 494 is larger, reflecting more friction, as there is significantly less water lubrication along the
 495 sides of the glacier compared to the base. Experimentation in Trantow (2014) suggests
 496 the lateral friction coefficient, $\beta = \beta_{lat}$, is 5 times larger than the nearest basal slid-
 497 ing coefficient based on observed velocities and shear behavior near the margins.

498 We treat the lateral margins uniformly throughout the entire glacier perimeter by
 499 assuming a rigid, mountainous boundary (with or without till). This representation, how-
 500 ever, does not hold for behavior at the glacier terminus. Calving at Bering Glacier's ter-
 501 minus is a complicated process somewhat unique among surge-type glaciers in that it
 502 calves into a series of proglacial lakes, the largest of which is Vitus Lake, rather than the
 503 ocean (Lingle et al., 1993). Throughout most of the surge cycle, the terminus is grounded
 504 at the lake bed being held down by the tensile strength of the ice. Unbalanced hydro-
 505 static pressure acting on the glacier bottom pushes upwards at the glacier front result-
 506 ing in a bending moment. The bending moment causes a fracture, likely at the point of
 507 maximum moment occurring at the glacier base, eventually leading to calving events.
 508 Since Bering Glacier is grounded below hydrostatic equilibrium, the icebergs pop up once
 509 calved, and float at a higher elevation than the grounded ice at the terminus. The calv-
 510 ing mechanism occurring during the surge phase is unknown but likely takes the form
 511 of an active calving cliff (Lingle et al., 1993).

512 We do not model Bering's complicated and changing calving process in this paper
 513 and instead treat mass loss from the system due to calving in the following manner. First,
 514 we extend the glacier model domain by several kilometers (2-5 km) at the glacier ter-
 515 minus assigning it the minimum ice thickness of 1 meter. The assumed true glacier ter-
 516 minus is derived from satellite imagery in 2016, marked by a solid black line in Figure
 517 6, while the extended model boundary is given by observations of the terminus at its max-
 518 imal extent after the most recent surge (Trantow, 2020). We treat all ice-mass that crosses
 519 into this extended region as ice lost to the system via calving. During the surge, the ice
 520 movement into this region may be seen as an approximate representation of terminus ex-
 521 tension, but without a retarding force due to lake water. The latest surge extended Bering's
 522 terminus 2-4 km (Turrin et al., 2013), therefore our region of minimum ice thickness is
 523 large enough to account for this phenomenon.

524 3.3 Hydropotential as a Proxy for Subglacial Drainage

525 Observations of subglacial hydrological systems are sparse, difficult to interpret and
 526 often do not provide the necessary information required to constrain parameters in a sub-
 527 glacial drainage model (Brinkerhoff et al., 2016; de Fleurian et al., 2018). Moreover, there
 528 are very few applications of subglacial hydrological models to real topographies and forc-
 529 ings due to the modeling difficulties (de Fleurian et al., 2018). The absence of any com-
 530 prehensive hydrological measurements for the BBGS, combined with the difficulty of ap-
 531 plying a sophisticated subglacial hydrological model to a large and complex glacier sys-
 532 tem, we choose to use a calculation of hydraulic potential (hydropotential) and its gra-
 533 dient to infer characteristics of the subglacial hydrological system throughout the surge
 534 cycle. We investigate the hydraulic gradient along the one-dimensional flowline whose
 535 coordinates are given x (see Fig. 3).

536 In this study we use the Shreve Potential (Equation 14) (Shreve, 1972) to estimate
 537 hydropotential and investigate evolution of glacial hydrologic characteristics through-
 538 out the surge cycle. More specifically, the gradient of hydropotential (hydraulic gradi-
 539 ent) is used as a steady-state proxy for water flow. Water is estimated to flow from ar-
 540 eas of high to low hydropotential in the direction of the (negative) hydraulic gradient.
 541 This approach has had success in predicting actual subglacial hydraulic characteristics
 542 (e.g., Sharp et al. (1993); Chu et al. (2016)). However, the calculation and subsequent
 543 analysis of the Shreve Potential requires several assumptions that are perhaps unreal-
 544 istic for actual glaciers, which we discuss here as we introduce the mathematics.

545 Given a certain glacier geometry, the hydropotential calculation is calculated by
 546 knowing the ice thickness and water pressure at some point within the glacier. The ex-
 547 pression for hydropotential Φ at the bed is given by,

$$548 \Phi = \rho_w g z_b + p_w \quad (13)$$

549 where ρ_w is the density of water, z_b the elevation of the bedrock and $p_w = \rho_i g h - N$
 550 the water pressure with ρ_i representing ice density and N effective pressure. Here we ar-
 551 rive at our first major assumption which assumes the effective pressure is zero everywhere,
 552 that is, the ice overburden pressure is approximately equal to the water pressure ($\rho_i g h \approx$
 553 p_w). This is only realistic if water completely fills the subglacial (or englacial) drainage
 554 conduit, and its enlargement rate is assumed to be the same at every location. During
 555 the surge, the rapid basal motion, due to increased basal water, implies an effective pres-
 556 sure at, or at least near, zero. Moreover, as shown in the flow-dynamic experiments in
 557 Trantow (2014), the quiescent phase velocities cannot be accurately captured without
 558 accounting for basal motion which also implies a very low effective pressure, making this
 559 assumption reasonable for the BBGS throughout most of its surge cycle as far as pre-
 560 dicting drainage paths goes.

561 With the $N = 0$ assumption, hydropotential can be calculated by,

562
$$\Phi = [\rho_i z_s + (\rho_w - \rho_i) z_b]g = \rho_i g h + \rho_w g z_b, \quad (14)$$

563 where $h = z_s - z_b$ is the height of the glacier. In this form, we see the hydropotential
564 is simply the combination of ice overburden pressure and the elevation (or topographic)
565 potential.

566 Aside from the zero effective pressure assumption, this formulation also assumes:
567 (1) the glacier ice and subglacial till have an intrinsic permeability that is homogenous
568 and isotropic, and (2) the recharge of water to the glacier bed is spatiotemporally uni-
569 form (Gulley et al., 2009, 2012). The spatiotemporal heterogeneity of both subglacial
570 water recharge, i.e., water entering the subglacial drainage system, and hydraulic con-
571 ductivity at the glacier bed have both been identified by Gulley et al. (2012) to be im-
572 portant components of estimating hydropotential, and they are not accounted for in the
573 formulation of Equation 14. However, given our available data sets and the usefulness
574 the Shreve potential approach to estimate subglacial drainage characteristics in some pre-
575 vious studies (Sharp et al., 1993; Chu et al., 2016), we proceed to estimate hydropoten-
576 tial using Equation 14 keeping in mind its assumptions and limitations.

577 **3.4 Surface Mass Balance Forcing**

578 Annual accumulation and ablation estimations for the BBGS are given by Tangborn
579 (2013) as a function of ice-surface elevation while Larsen et al. (2015) provide SMB rates
580 for glaciers across Alaska, including the BBGS. Tangborn (2013) employs a PTAA (precipitation-
581 temperature-area-altitude) model, using daily precipitation and temperature observa-
582 tions from nearby weather stations to derive historical net ablation and accumulation
583 balances with respect to ice-surface altitude from 1951-2011. More recently, Larsen et
584 al. (2015) used airborne altimetry to estimate regional mass balances for Alaskan moun-
585 tain glaciers. The rates given by Tangborn (2013) estimate much higher melt-rates for
586 the BBGS which are at odds with the more recent and comprehensive measurements by
587 Larsen et al. (2015). We therefore enforce accumulation and ablation rates whose mag-
588 nitudes better reflect those measured by Larsen et al. (2015), but still employ the quasi-
589 linear relationship of SMB rates with respect to ice-surface altitude derived by Tangborn
590 (2013).

591 Figure 5 shows the linear relation between our enforced SMB and ice-surface el-
592 evation. A histogram describing the distribution of ice-surface elevation at each model
593 surface-node throughout the BBGS is also shown in the same plot. The slope of the line
594 is derived from a linear approximation, fit in a least-squares sense, of the mean net mass
595 balance for the BBGS from 1951-2011 converted to meters per year of ice from the orig-
596 inal mean-water-equivalent per year in Tangborn (2013). This conversion requires an as-
597 sumption of constant ice density which is set at 917 kg/m^3 (ice density for the 0°C isother-
598 mal assumption). The y-intercept is adjusted so that the function spans the observed
599 range given by Larsen et al. (2015). SMB forcing is applied uniformly in a temporal sense
600 and does not account for seasonal variability in accumulation or ablation.

601 The equation for enforced annual mean-SMB (in terms of meters of ice gain/loss),
602 smb_{mean} , is given by glacier surface elevation z :

603
$$smb_{mean} = (0.0015 \cdot z - 2) / 0.917 \quad (15)$$

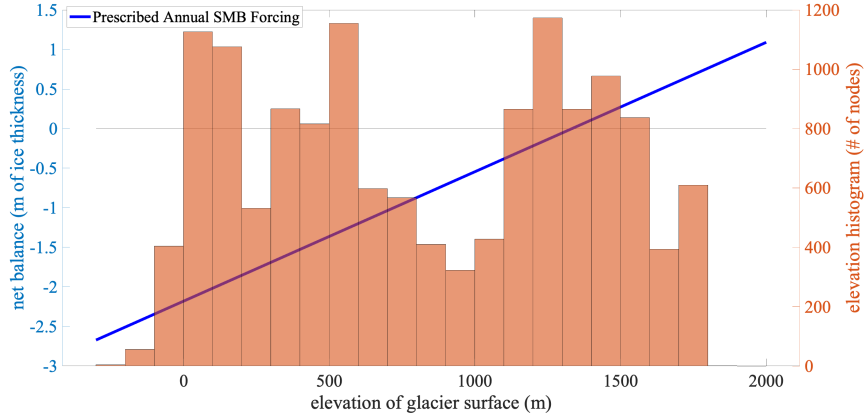


Figure 5. Annual net surface mass balance estimates for Bering Glacier as a function of elevation derived from Larsen et al. (2015) and Tangborn (2013). The blue line gives the linear approximation of relationship between glacier surface elevation and surface mass balance based on Tangborn (2013) while the magnitude of surface mass balance is based on Larsen et al. (2015). The histogram shows the distribution of model surface-nodes at a given elevation throughout the BBGS at the beginning of quiescent phase experiment (Summer 2016 geometry).

4 The Quiescent Phase

Prognostic simulations of the entire quiescent phase help identify how mass is redistributed in the BBGS over the course of normal flow, which leads to conditions favorable for surging. After providing some model specifics for the quiescent simulation, we analyze the mass redistribution results and estimate mass loss over 20-years of quiescent flow (Section 4.1). Next we infer changes in the basal hydrological system caused by the mass redistribution through calculation of the subglacial and englacial hydraulic gradients (Section 4.2). We then identify reservoir areas and associated subglacial topography characteristics that are responsible for the observed changes in Section 4.3. Finally, we compare simulated and observed velocity during quiescence and propose a way to increase complexity of the quiescent phase friction law to better match observations in Section 4.4.

We simulate quiescent flow for 20 years using 10-day time increments (730 total time steps), which corresponds to the approximate length of the observed BBGS quiescent phases since 1900 (B. F. Molnia & Post, 2010). While the most recent quiescent phase, beginning in 1996, lasted only 12-15 years, the results in this section remain applicable as changes during quiescent flow are gradual and evolve monotonically. The magnitude of changes expected during the last full quiescent phase however, might not be as dramatic as at given by the 20-year results given in this section.

4.1 Elevation Change and Mass Loss

Figure 6(a) shows quiescent elevation change by differencing the initial surface elevation with the surface elevation after 20 years of evolution. The initial ice surface is taken as the glacier surface after 50 time steps of free evolution in order to reduce any elevation-change signals arising from errors in the input surface DEM (Trantow et al., 2020).

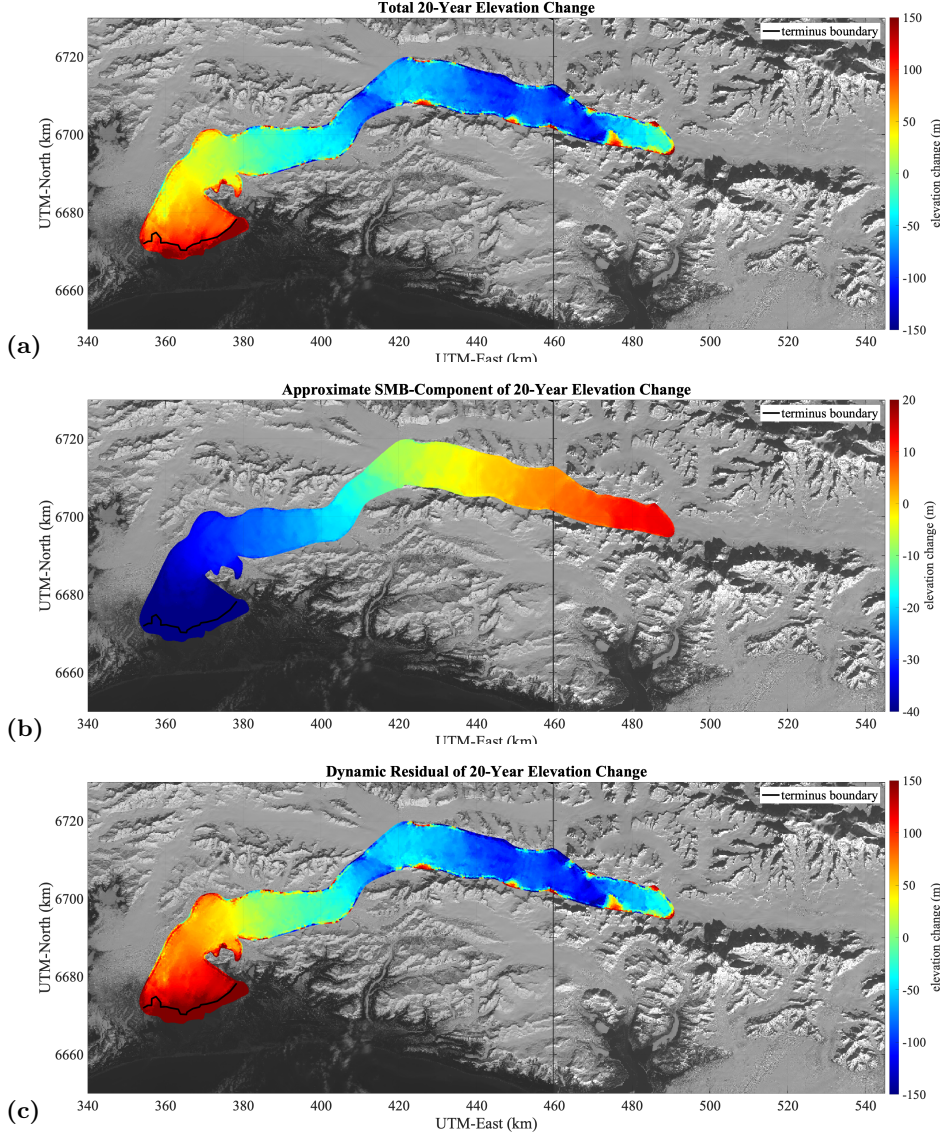


Figure 6. Elevation change results from 20-year quiescent simulation of the BBGS.

(a) Total elevation change in meters. (b) Approximate SMB component of elevation change.

(c) Approximate dynamic component of elevation change. The black line marks the assumed glacier terminus, derived from the observed 2016 boundary, and is treated as a flux gate to estimate calving.

Figure 6(b) shows the approximate contribution of SMB forcing on the overall quiescent elevation-change signal. The approximation is calculated by applying the SMB rate to the initial topography aggregated for 20 years (the true SMB signal changes at each time step due to a redistribution of ice-surface elevation). With our enforced accumulation/ablation pattern, based on observations in the current realm of climatic warming, it is not surprising that the overall glacier system loses mass. We see accumulation up to 20 m throughout most of the Bagley Ice Field with significant melt rates throughout Bering Glacier and the lower Bagley exceeding 30 meters near Bering's terminus. These rates lead to a total estimated mass loss signal of 25.21 km^3 from SMB over the 20-year simulation (1.363 km^3 per year).

639 Subtracting the SMB signal from the total simulated elevation-change we receive
 640 the dynamic-residual, i.e., the elevation change signal from the dynamics of the glacier
 641 (Figure 6(c)). Clearly, the total elevation-change signal is dominated by the dynamics
 642 of the glacier which is expected for the relatively fast-moving temperate glaciers of south-
 643 east Alaska. Ice loss due to dynamics comes in the form of calving which we estimate
 644 as mass passing past the flux-gate marking the initial terminus (black line in Figure 6(c))
 645 and into the extended region at the front of the glacier (see Section 3.2.3). Over the course
 646 of the 20 year quiescent phase, we estimate 12.88 km^3 of mass loss due to calving in the
 647 BBGS (0.644 km^3 per year). Thus, the combined mass loss is approximately 38.09 km^3
 648 for 20 years (1.90 km^3 per year) with SMB contributing to $2/3$ of the signal and mass
 649 loss due to dynamics (calving) contributing to $1/3$.

650 4.2 Hydropotential Analysis

651 We use hydropotential to infer characteristics of the subglacial drainage system that
 652 result from changing geometries, as described in Section 3.3, which is an important as-
 653 pect in understanding surge evolution. Maps of hydropotential provide estimates for the
 654 path that water takes through the ice-bed interface as it drains to the glacier terminus,
 655 flowing down the hydraulic gradient from high to low (hydro)potential.

656 The basal hydropotential depends on local ice thickness and can therefore deviate
 657 from the topographic gradient of the bedrock, that is, the accumulation of ice in reser-
 658 voir areas during quiescence changes the basal hydraulic gradient. In general, the steeper
 659 the surface slope, the less the glacial drainage flows along the local bed topography (Shreve,
 660 1972). Therefore, we expect the glacier steepening near the reservoir areas to divert the
 661 flow of water at the base from its early-quiescent path.

662 Figure 7 gives a full spatial map of the basal hydropotential of the BBGS in year-
 663 1 and year-20 of the quiescent simulation. Colored contours are given at 0.2 MPa in-
 664 tervals while black labeled contours are given at 1.6 MPa intervals. The general direc-
 665 tion in which water flows will be perpendicular to the equipotentials of the hydropoten-
 666 tial. Subglacial water storage occurs in closed areas of lower hydropotential (hydropo-
 667 tential wells), similar to ordinary lakes forming in closed areas of lower elevation (Shreve,
 668 1972).

669 These maps indicate that the efficiency of the hydraulic drainage throughout Bering
 670 Glacier's trunk, given by the amount of contours per distance along the flowline, is much
 671 lower in year-20. The 1.6 MPa black reference lines are given in the figure to help high-
 672 light this change. Moreover, we see the development of potential wells throughout Bering
 673 Glacier as indicated by the arrows in Figure 7(b).

674 To better visualize and quantify these subglacial drainage changes in Bering Glacier's
 675 trunk, we created along-flowline plots of the hydropotential and hydropotential gradi-
 676 ent by averaging the values across the glacier width. Figure 3 gives a reference to the
 677 along-flowline distance starting at the uppermost accumulation zone near the Eastern
 678 Bagley Ice Field's confluence with Columbus Glacier, and ending $\sim 157 \text{ km}$ down glacier
 679 at Bering's terminus. Note however, that labeling this the flowline is somewhat mislead-
 680 ing as several flow regimes exist and multiple subglacial troughs divide the flow across
 681 the glacier width, especially near the lobe area past the 125 km mark (B. F. Molnia &
 682 Post, 2010; Trantow, 2020).

683 Figure 8(a) shows the mean along-flowline elevation (dashed) and hydropotential
 684 (solid) at the beginning (red) and end (blue) of the quiescent experiment over the trunk
 685 of Bering Glacier (km-80 to km-135). Note that it is the *difference* in hydropotential,
 686 across some fixed distance, that is the salient measure of hydraulic flow efficiency rather
 687 than the magnitude of hydropotential at some location. We therefore analyze the dif-
 688 ference in hydropotential across Bering Glacier's trunk which has decreased by 16.6%

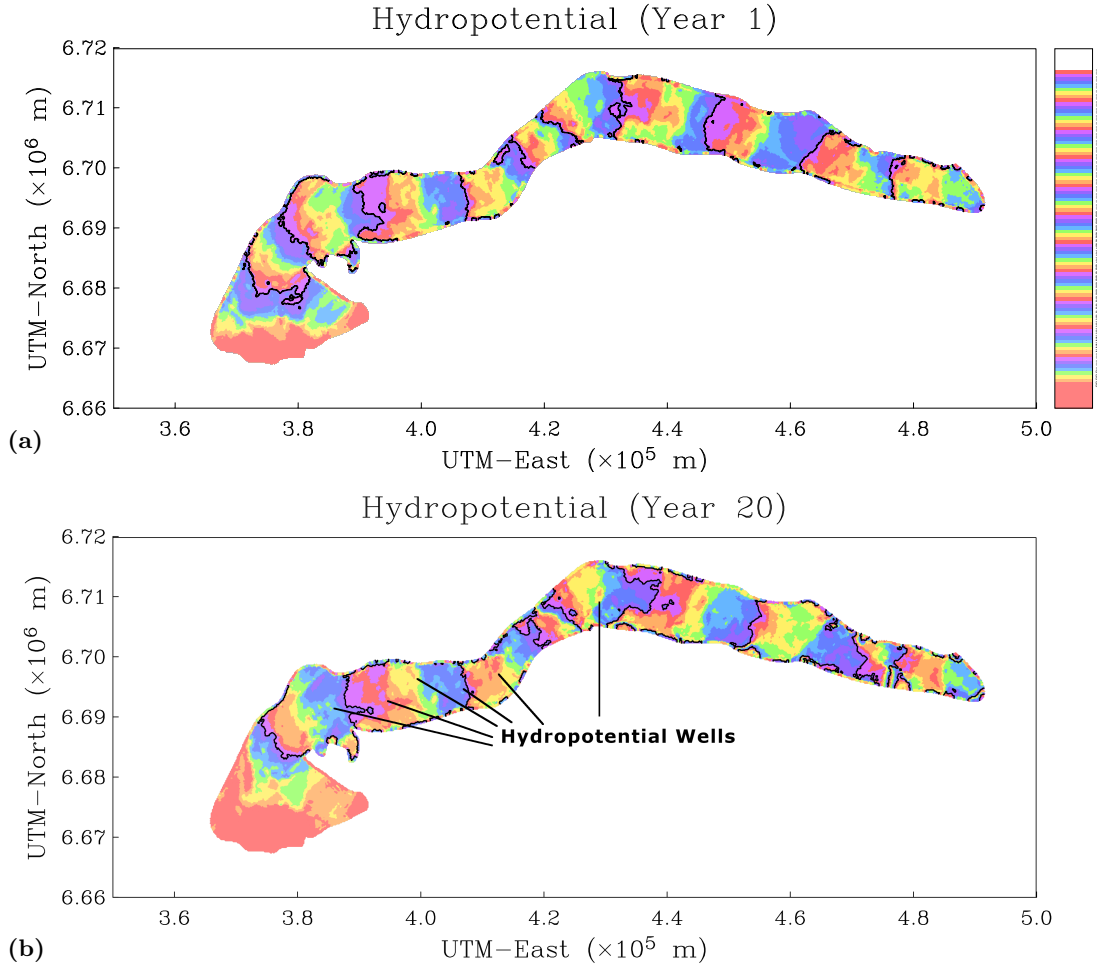


Figure 7. Modeled basal hydropotential for at the beginning and end of the 20-year quiescent phase simulation of the BBGS. Colored contours are given at 0.2 MPa intervals while black-lined contours are given at 1.6 MPa intervals. (a) Basal hydropotential for at the beginning of the quiescent phase in year 1. (b) Basal hydropotential at the end of a 20-year quiescent phase. The black lines indicate notable hydropotential-wells that have grown or developed over the course of 20-years of quiescent flow.

over the course of quiescence. Even without considering the existence of hydropotential wells, this result suggests that Bering Glacier's trunk is draining basal water less efficiently down-glacier, with more transverse drainage paths, assuming a fixed water inflow rate.

Figure 8(b) shows the mean along-flowline hydraulic gradient of Bering Glacier's trunk over the course of quiescence, indicating drainage rates down-glacier and locations where Bering Glacier is storing basal water as indicated by a positive hydraulic gradient. Clearly, the amount of water being stored at the end of quiescence (blue solid line above 0, shaded for clarity) has increased significantly from the beginning of quiescence (red solid line). The amount of water stored in the hydropotential wells, as estimated by the area of each line above zero, has increased by 246% over the course of quiescence. These well-areas, and other areas where the hydraulic gradient is less than zero along the flowline, correspond to the surge "trigger zones" identified in Robin and Weertman

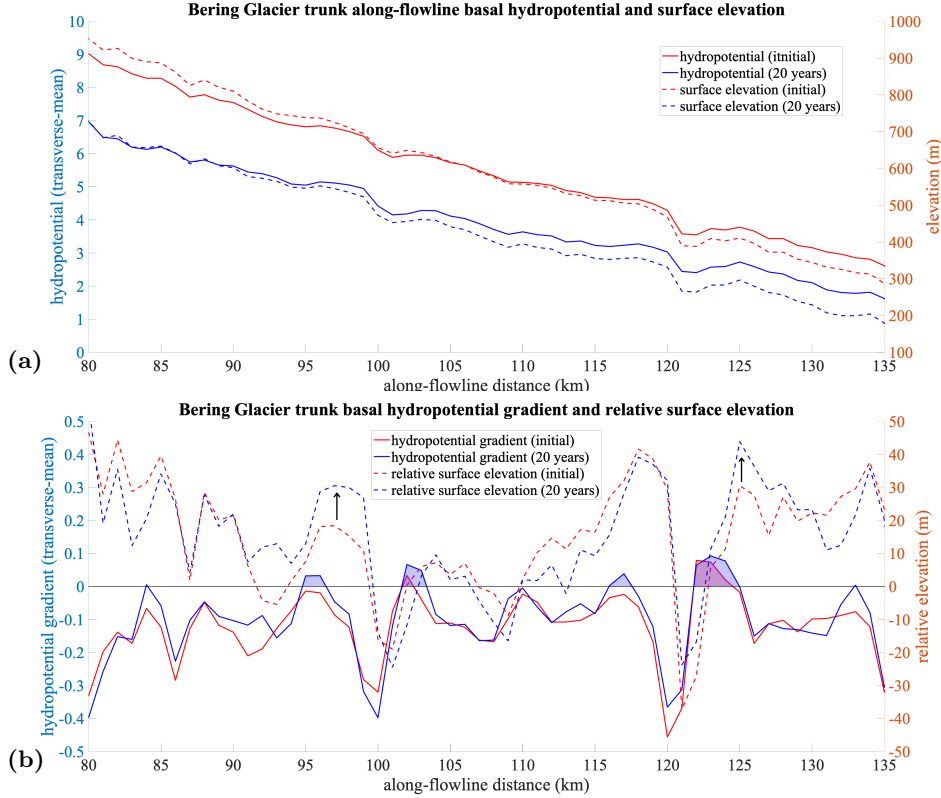


Figure 8. Change across the Bering Glacier trunk with regards to hydropotential and surface elevation over the course of the modeled quiescent phase. Red lines reflect the glacier state at the beginning of quiescence while blue lines reflect the end of quiescence state. (a) Hydropotential (solid lines) and surface elevation (dashed lines). (b) Hydropotential gradient (solid lines) and relative surface elevation (dashed lines). Relative surface elevation is calculated by removing the mean slope of surface elevation. Shaded areas reflect locations where the hydropotential gradient is above zero implying water flowing up-glacier, i.e., subglacial water storage. Black arrows indicate growing surface bulges.

(1973) where basal water is “dammed” increasing stored water in the up-glacier zones where the hydraulic gradient is near-zero, which corresponds to the “collection areas”.

The dashed lines in Figure 8(b) show the relative elevation initially (red) and after 20-years of quiescent flow (blue). Relative elevation is found by subtracting the mean slope from the elevation profiles in Figure 8(a) and indicates where reservoir areas, or surface bulges, are forming. The black arrows around km-97 and km-123 indicate building reservoir areas, while the high relative-elevation area around km-118 retains a fixed magnitude throughout the quiescent phase while steepening on its up-glacier-side. The enlarging reservoir areas and steepening of local geometry lead to increased stored water in the areas 2-4 km up-glacier of these bulges. We also identify an area of stored water around km-102 without a large corresponding surface bulge, however, the relative surface slope in this area is steepening.

4.3 Reservoir Areas and Bedrock Topography

The locations of the reservoir areas, along with the basal water storage areas, are attributed to the characteristics of Bering Glacier’s bedrock topography, shown in Fig-

ure 9(a), whose shape is influenced by the local faults (Koehler & Carver, 2018; Trantow, 2020). In particular, it is the extension of the surrounding mountain ridges underneath the glacier, termed “subglacial ridges”, that are responsible for damming ice at these locations. Black arrows in Figure 9 point out some of the significant subglacial ridges. Directly up-glacier of these ridges are local deepenings in the basal topography where water collects. Ice-mass build-up in front of these deepenings, caused by the subglacial ridges, slows the down-glacier drainage resulting in increased water retention in this area as shown in Figure 8(b).

The 3 reservoir areas we have identified through our quiescent phase simulation are circled in red in Figure 9(a) and the four areas of subglacial water storage are circled in dark purple. These areas are possible locations where surge initiation (or re-initiation) occurs, likely at the down-glacier edge of the reservoir areas where ice-surface geometry is steepest. The reservoir area centered at km-97 with a leading edge at km-100, termed RA-97, is identified by Burgess et al. (2013) to be the reservoir area for the initial surge phase in early-2008, which, after mass transfer to the receiving areas, likely caused the observed rift in the former receiving area (U. Herzfeld, 1998; U. C. Herzfeld et al., 2013; Trantow, 2020). D. R. Fatland and Lingle (2002) hypothesize that RA-97 is the reservoir area for the 1993-1995 surge of Bering Glacier. RA-97 is formed by two transverse pairs of subglacial ridges just up-glacier of Ovtsyn Glacier on the north margin and just down-glacier of Kuleska Glacier on the south margin. Ice-mass accumulates behind the ridges, filling the deep bedrock depression, giving the thickest ice in all of Bering Glacier.

The reservoir area centered at km-124 with a leading edge at km-126, termed RA-124, is identified as the reservoir area in 2010/2011 by U. C. Herzfeld et al. (2013) for the major surge phase occurring in early 2011, who measured a prominent surface lowering at this location of over 50 m in the summer of 2011 indicating a bulge collapse after the surge had been progressing for several months. Down-glacier of RA-124 in the Bering lobe is an area of complex topography where the deep trough running through Bering’s trunk splits into two major branches, which we term the Tashalish Trough in the west and the Grindle Trough in the east, with even more subglacial troughs appearing further down-glacier in the lobe area. The Khitrov and Grindle Hills on the north and south side of the glacier respectively, produce large subglacial ridges that serve to accumulate ice before it crosses the Khitrov-Grindle line by flowing down a particularly steep section of bedrock into the lobe area. This steep slope, identified along the Grindle Corner in aerial imagery by a series of ice falls (U. C. Herzfeld et al., 2013; Trantow & Herzfeld, 2018), explains why the surge wave, as measured by Turrin et al. (2013), speeds-up once it reaches this area.

Subglacial ridges that continue from nearby mountain ridges are also frequent in the Bagley Ice Field, as seen in Figure 9(b), causing ice-mass build-ups directly up-glacier (specifically near km-64, km-41, km-31, km-23, km-12 and km-3). Their existence in the BIF is evident from the topographically induced en-échelon crevasses (Figure 2(f)) (U. C. Herzfeld & Mayer, 1997; U. C. Herzfeld et al., 2013).

The Bagley Ice Field does not experience a full-scale surge of its own due to a lack of melt-water throughout the ice field. As seen in our SMB prescription (Figures 5 and 6(b)), along with Larsen et al. (2015), most of the Bagley Ice Field lies in the accumulation zone of the glacier system and experiences minimal surface melt throughout the year. The lower part of the Bagley Ice Field does experience significant melt with a net-negative SMB balance down-glacier of km-60. The reservoir area at km-64 (RA-64) coincides in location with a small acceleration event (mini-surge) identified by Burgess et al. (2013) that occurred in the Bagley Ice Field during quiescence in 2003. Based on the local basal topography, the released basal water during the mini-surge event would divert northwest through Tana Glacier, quickly exiting the subglacial drainage system, and little basal water would be expected to flow across the BBJ into Bering Glacier. Tana Glacier is significantly shorter and thinner than Bering Glacier, with shorter water drainage

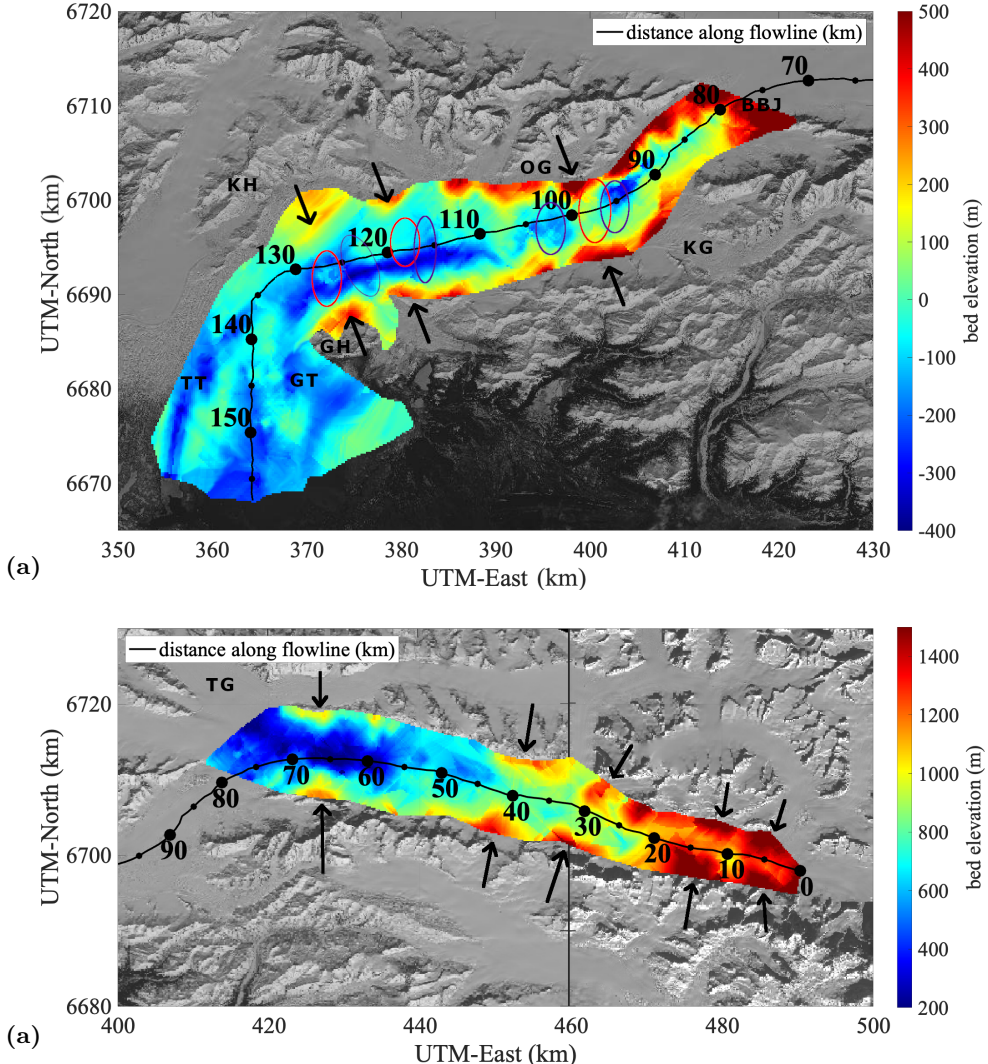


Figure 9. Locations of estimated reservoir areas and water storage over bedrock topography for Bering Glacier and the Bagley Ice Field. The along-flowline distance is given by the black line (km) while black arrows indicate subglacial features that contribute to the formation of the reservoir areas. a) Bering Glacier bedrock topography. Possible reservoir areas are circled in red and water storage areas are circled in dark purple. (b) Bagley Ice Field bedrock topography with notable subglacial ridges indicated by arrows. BBJ – Bering-Bagley junction, TG – Tana Glacier, KG – Kuleska Glacier, OG – Ovtsyn Glacier, TT – Tashalish Trough, GT – Grindle Trough, KH – Khitrov Hills, GH – Grindle Hills.

769 passageways, and can evolve more readily to accommodate up-glacier changes in mass
 770 and water flux. Tana Glacier is not observed to surge (Burgess et al., 2013), and thus
 771 mass imbalances and water retention likely do not occur on the scale that they do in
 772 Bering Glacier.

773 Lingle and Fatland (2003) describe velocities in the BIF during the 1993-1995 BBGS
 774 surge using SAR interferometry and found a large “bullseye” at the location of RA-64.
 775 The bulls-eye corresponds to englacial water build-up that had caused vertical motion
 776 in the glacier during the 1993-1995 BBGS surge. Due to RA-64’s location just above the

777 BBJ, hydraulic changes experienced here may have some affect on Upper Bering Glacier
 778 where the surge is thought to initiate.

779 4.4 Velocity and Friction Law Improvements for the Quiescent Phase

780 We compare modeled velocity to observed velocity during the quiescent phase in
 781 order to (1) check that our modeled velocity is close to observations and (2) use the dif-
 782 ferences to suggest ways to improve the quiescent phase modeling. Figure 10(a) gives
 783 the observed mean annual velocity across the BBGS from 2020-03-08 to 2021-03-03 as
 784 derived from Sentinel 1A imagery using the SNAP toolbox (provided for analysis of SAR
 785 data by ESA,(Veci et al., 2014)). We see that most of the glacier system moves at a rate
 786 less than 0.5 m/day, but there are pockets of accelerated flow throughout that reach up
 787 to 5 m/day. These pockets coincide with the areas of water retainment identified in the
 788 previous section. This result suggests that the observed acceleration pockets are corre-
 789 lated with local hydraulic drainage inefficiencies leading to low effective pressures. Maps
 790 during other years of quiescence show similar patterns (Trantow (2020), Chapter 4.2).

791 Figure 10(b) gives the modeled velocity near the end of quiescence at the same scale
 792 as the observed velocity in (a). Similar to observations, our model predicts that most
 793 of the glacier moves slower than 0.5 m/day, with areas of accelerated flow. The areas of
 794 accelerated flow however, do not directly coincide with observations. Figure 10(c) shows
 795 the observed velocity minus the modeled velocity with a mean difference of -0.21 ± 0.63
 796 m/day across the BBGS.

797 Figure 10(d) plots the along-flowline velocity difference (blue) averaged across the
 798 glacier width versus the smoothed hydraulic gradient along-flowline (red). The hydraulic
 799 gradient is smoothed across a 5 km length to avoid high frequency signals that may re-
 800 sult from errors in the basal topography. We find that the hydraulic gradient at loca-
 801 tions in Bering Glacier and lower Bagley, i.e. the ablation zone down-glacier of km-65,
 802 coincide remarkably well with the difference between observed and modeled velocity. That
 803 is, locations where our model over-estimates surface velocity the hydraulic gradient is
 804 relatively low and vice versa. A similar relationship holds for the accumulation zone in
 805 mid and upper Bagley, but the proportionality constant is different likely owing to the
 806 fact that there is less basal water present.

807 Such a clear relationship between the hydraulic gradient and velocity discrepan-
 808 cies leads us to investigations of a quiescent phase friction law that depends on the gra-
 809 dient of hydropotential, i.e.,

$$810 \beta = \beta(\nabla\Phi) \quad (16)$$

811 where β is the linear friction coefficient from Equation 9 and $\nabla\Phi$ is the hydraulic gra-
 812 dient. Here, the easy to calculate hydraulic gradient would be a proxy for the effective
 813 pressure, N , which is difficult to measure as it depends of basal water pressure. Such a
 814 law for the BBGS quiescent phase could start with a uniform friction coefficient equal
 815 to $10^{-4} \frac{MPa \cdot a}{m}$ as we do in our simulations here, with adjustments to this value occur-
 816 ring throughout the model run based on the calculated hydropotential. The inclusion
 817 of hydropotential calculations would also improve the surge-wave friction law (Equation
 818 12) which is based on the linear friction law used during quiescent simulation. We leave
 819 further investigations of this type to later studies and proceed to model the initial surge
 820 phase of the BBGS in the next section.

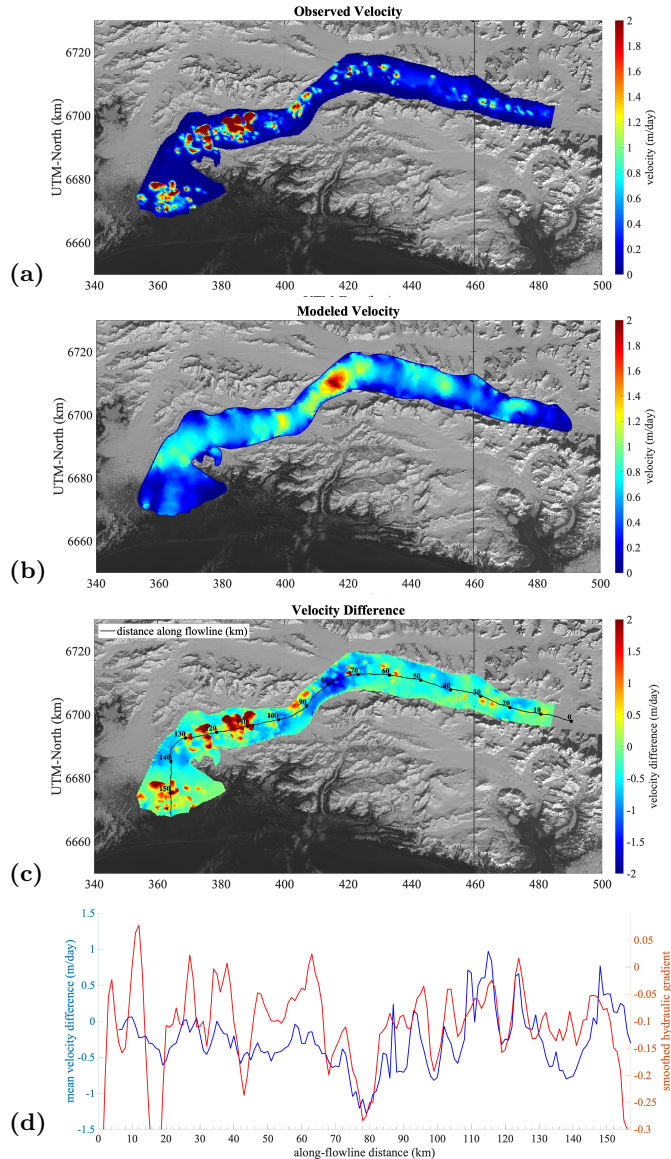


Figure 10. Observed and modeled ice-surface velocity during the BBGS quiescent phase. (a) Observed velocity derived from Sentinel-1 SAR imagery (S1A, 2020-03-08 and 2021-03-03). (b) Modeled velocity near the end of quiescence. (c) Observed-modeled velocity difference with along-flowline distance plotted in black (observed minus modeled). (d) Mean velocity difference (blue) and smooth hydraulic gradient (red) along-flowline.

821 5 The Surge Phase

822 As mentioned previously, the model simulates glacier dynamics using a 3D full-stokes
 823 representation since we do not wish to impose any stress-related assumptions on the glacier,
 824 especially during the surge when rapid deformation of ice occurs in all three spatial di-
 825 mensions. Our computational resources at the time of analysis however, are limited and
 826 therefore we decided to model only the ~2-year initial surge acceleration as it progresses
 827 through the trunk of Bering Glacier (corresponding to the 2008-2010 phase of the most
 828 recent surge). A full-Stokes simulation of the full surge phase that includes the second
 829 surge phase, most recently occurring in 2011-2013, is calculated more feasibly using high-
 830 performance computing which is left for future work. In the mean time, we supplement
 831 interpretation of the the second surge phase and the return to quiescence using observed
 832 CryoSat-2 Digital Elevation Models and Landsat-derived velocity maps from 2011 and
 833 2013 (Trantow & Herzfeld, 2016).

834 In this surge phase section, we begin by providing several surge initiation criteria
 835 in Section 5.1 based on the results of the quiescent phase experiments which could serve
 836 to link quiescent and surge simulations in future experiments. Next, we present the re-
 837 sults of our two-year surge-simulation of the BBGS's initial surge phase given by a surge-
 838 wave propagating trough Bering Glacier's trunk in Section 5.2. We present results of mod-
 839 eled velocity (Section 5.2.1), basal shear stress (Section 5.2.2), elevation change (Section
 840 5.2.3) and hydropotential (Section 5.2.4) at various time stamps throughout the sim-
 841 ulation. Finally, in order to complete our picture of the surge past the initial phase, we
 842 use CryoSat-2 observations in Section 5.3 to analyze mass redistribution and hydraulic
 843 drainage efficiency during the 2011-2013 phase of the most recent BBGS surge (second
 844 surge phase) ending with the transition back to a quiescent state (Section 5.4).

845 5.1 Surge Initiation

846 One of the least understood mechanisms of surging is surge-initiation. In this sec-
 847 tion we investigate our end-of-quiescent results to identify glacier conditions that would
 848 initiate a surge. The traditional surge hypothesis states that surges are triggered due to
 849 an internal change in the system such as the collapse of an EDS (Meier & Post, 1969;
 850 Clarke et al., 1984; Raymond, 1987; Harrison & Post, 2003). Trantow (2020) showed that
 851 surge initiation of the last three BBGS surges showed no clear correlation with nearby
 852 precipitation and temperature anomalies as measured by the nearby Cordova weather
 853 station. We therefore use particulars of the glacier geometry and the basal drainage sys-
 854 tem, via hydropotential analysis, to derive a surge-initiation criterion as justified in the
 855 following.

856 A changing glacier geometry over quiescence leads to stress conditions that can cause
 857 sudden changes in the glacier drainage system (Robin, 1969). An EDS can be destroyed
 858 when large overburden pressures from a growing reservoir area overcome the low water
 859 pressures experienced by temperate glaciers during the winter season. An IDS then de-
 860 velops up-glacier of the collapse. As melt water input begins to increase in late winter,
 861 water pressure increases throughout the IDS which spans the entire width due to restric-
 862 tive down-glacier drainage (W. Kamb et al., 1985; W. B. Kamb, 1987). If the IDS per-
 863 sists, the rising water pressure will eventually leads to surging, either through a total de-
 864 coupling of the ice from the hard bed or through dilation of the subglacial sediment (W. B. Kamb,
 865 1987; Truffer et al., 2000; Flowers & Clarke, 2002a, 2002b; Fleurian et al., 2014). Note
 866 that an EDS collapse and an IDS formation may occur without resulting in a surge if
 867 the EDS can recover before the water pressure reaches a critical level. The recovery time
 868 allowed before surging occurs however, becomes shorter with the growing amount of stored
 869 water up-glacier of the EDS collapse. That is, lower effective pressures across the glacier
 870 width in these areas are achieved quicker this time of year as the quiescence phase ma-
 871 tures.

872 An EDS collapse is likely to occur at locations with steep hydraulic gradients where
 873 water is least likely to accumulate and maintain the water pressure for a functioning drainage
 874 channel (W. Kamb et al., 1985; W. B. Kamb, 1987). As seen in Figure 8(b), the steepest
 875 (and negative) hydraulic gradients are modeled near the leading edge of the reser-
 876 voir area bulges, particularly at km-100 and km-120. We see that the growing reservoir
 877 area at km-97, with a leading edge around km-100, causes a steeper hydraulic gradient
 878 to develop near the leading edge while the gradient gets less steep at the km-119 reser-
 879 voir area where the shape of the leading edge remains relatively constant. The initial surge
 880 was observed to trigger near km-97 to km-100 in the latest surge Burgess et al. (2013),
 881 and for the purposes of this paper we trigger the surge simulation at this location after
 882 the 20 year quiescent evolution.

883 For future simulations that run over the course of an entire surge cycle, we would
 884 adopt a deterministic or probabilistic model to determine when and where the surge would
 885 be triggered though this task is made difficult with little to no subglacial or hydrolog-
 886 ical measurements. For example, a simple deterministic estimation of surge initiation based
 887 on our hydropotential results could be made by setting a threshold on the amount of sub-
 888 glacial water storage up-glacier of an increasingly steep hydraulic gradient. Alternatively,
 889 instead of a purely deterministic surge initiation criterion, a probabilistic method could
 890 be adopted whose density function is based on the hydraulic gradient.

891 5.2 Surge Simulations

892 In this section, we present the results from the \approx 2-year early-surge simulation ap-
 893 plied to the modeled end-of-quiescence geometry using the surge-wave friction law pro-
 894 posed in Section 3.2.2.2. Based on observations of the surge wave during the latest surge
 895 by Turrin et al. (2013), we set the surge-wave propagation speed to $u_{sf} = 50$ m/day
 896 (18.25 km/year) and as mentioned in the previous section, we set the along-flowline surge
 897 initiation location to $x_{init} = 100$ km, i.e., at the leading edge of RA-97. We use 132
 898 5-day time steps and do not include SMB forcing due to the short length of the exper-
 899 iment. The presented surge experiment models only the surge progressing through the
 900 mid to lower Bering Glacier trunk and corresponds to roughly the first two years of the
 901 surge (corresponding to \sim 2008 through 2010 of the latest BBGS surge).

902 5.2.1 Velocity

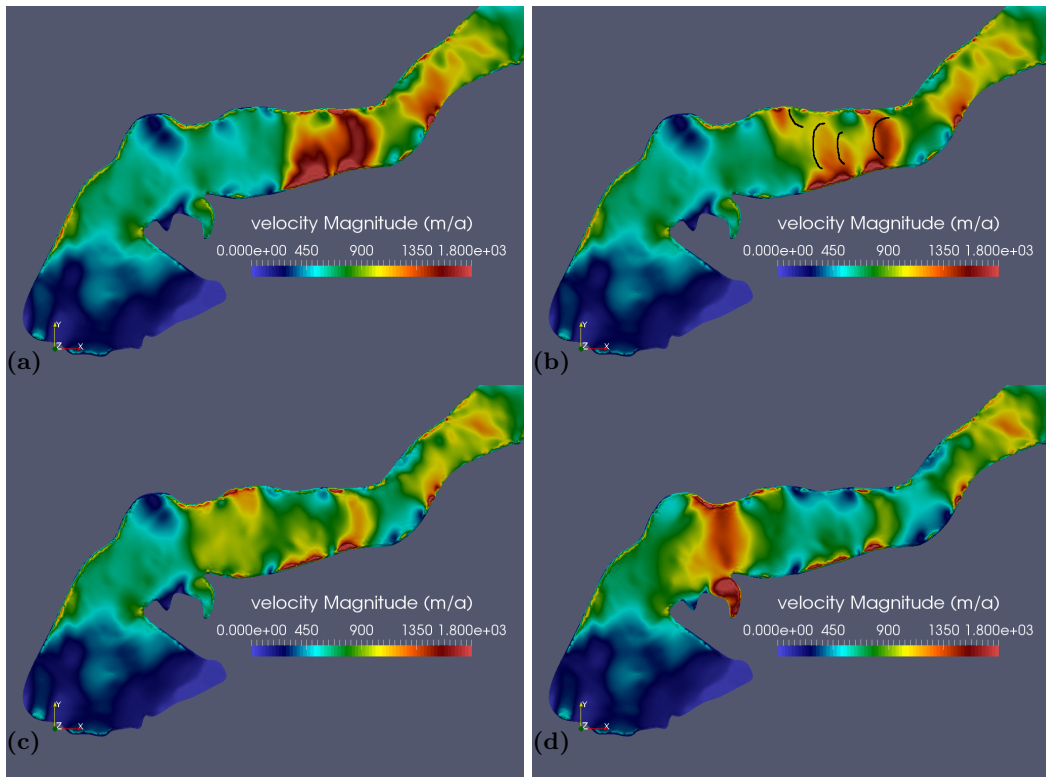
903 Figure 11 displays the surface velocity at various times during the simulated surge
 904 through Bering's trunk. Near the beginning of the simulation, when the surge has only
 905 affected a portion of the glacier (from km-100 to km-110), large surface velocities exceed-
 906 ing 1800 m/year (\sim 5 m/day) are identified. The fastest speeds at this time reach 10.25
 907 m/day which is similar to maximum observed velocities in this area given by Burgess
 908 et al. (2013) of 9 m/day. At later time steps, when the surge is progressing down-glacier,
 909 velocities subside in this area. When the surge front is moving through the thick ice along
 910 km-110 to km-120 (subfigure (c)), modeled ice-surface velocities are noticeably reduced
 911 with no areas of the glacier away from the margins exceeding 1000 m/year. This area
 912 of thick ice contained relatively few surge crevasses compared to the rest of Bering's trunk
 913 (Trantow & Herzfeld, 2018).

914 Burgess et al. (2013) observed that the surge appeared to subside between the ini-
 915 tial acceleration in 2008 (initial surge phase) and the reinitiation in 2011 (second surge
 916 phase). Our simulation here, however, shows that while the surge kinematic wave con-
 917 tinues to progress down glacier, ice-surface speeds will lessen when propagating through
 918 the thick ice between km-110 and km-125.

919 In addition, we also observe similar spatial velocity patterns in Bering's trunk be-
 920 tween our modeled velocities and the maps produced by Burgess et al. (2013) for 2010.

921 Burgess et al. (2013) labels the areas of high velocity in Central Bering as “surge fronts”,
 922 however, our model shows that these spatial patterns are persistent across the surge phase.
 923 The assumed surge fronts in Figure 3 of Burgess et al. (2013) are transposed on our mod-
 924 elled velocity map in Figure 11(b). Our results indicate that these high-velocity areas in
 925 Central Bering are not associated with surge fronts but are rather attributed to partic-
 926 ulars of the local bedrock topography.

927 Near the end of the simulation, when the surge front has reached km-125, peak mod-
 928 eled velocities begin to once again increase, reaching maximums near 10 m/day (exclud-
 929 ing modeled velocities in the overflow area, which are likely unrealistic). The modeled
 930 peak velocities in this area are consistent with those derived from the velocity map pre-
 931 sented in Trantow and Herzfeld (2018). The simulation ends as the surge wave reaches
 932 the final reservoir area near km-128 approximately 2 years after surge initiation.



933 **Figure 11. Modeled surface velocity throughout a short surge simulation.** Velocity
 934 given in meters per year. (a) Velocity at time step 10, (b) velocity at time step 40 with the
 935 “surge fronts” assumed by Burgess et al. (2013) marked in black, (c) velocity at time step 80 and
 936 (d) velocity at time step 132.

937 5.2.2 Basal Shear Stress

938 Figure 12 gives the modeled basal shear stress (in the x , or along-flow, direction)
 939 at the same time stamps above. The surge front is clearly marked in each subfigure as
 940 a dividing line between low basal shear stresses up-glacier (white/yellow) and high basal
 941 shear stresses down-glacier (orange/red) of the surge front. This figure reveals that basal
 942 shear stresses are reduced far up-glacier, well above the initiation location at km-100,
 943 where quiescent basal friction parameters still apply. This result reflects observations of
 944 a surge wave that propagates down-glacier also having effects that propagate up-glacier

941 into regions that are necessarily affected by local changes in basal drainage characteristics.
 942

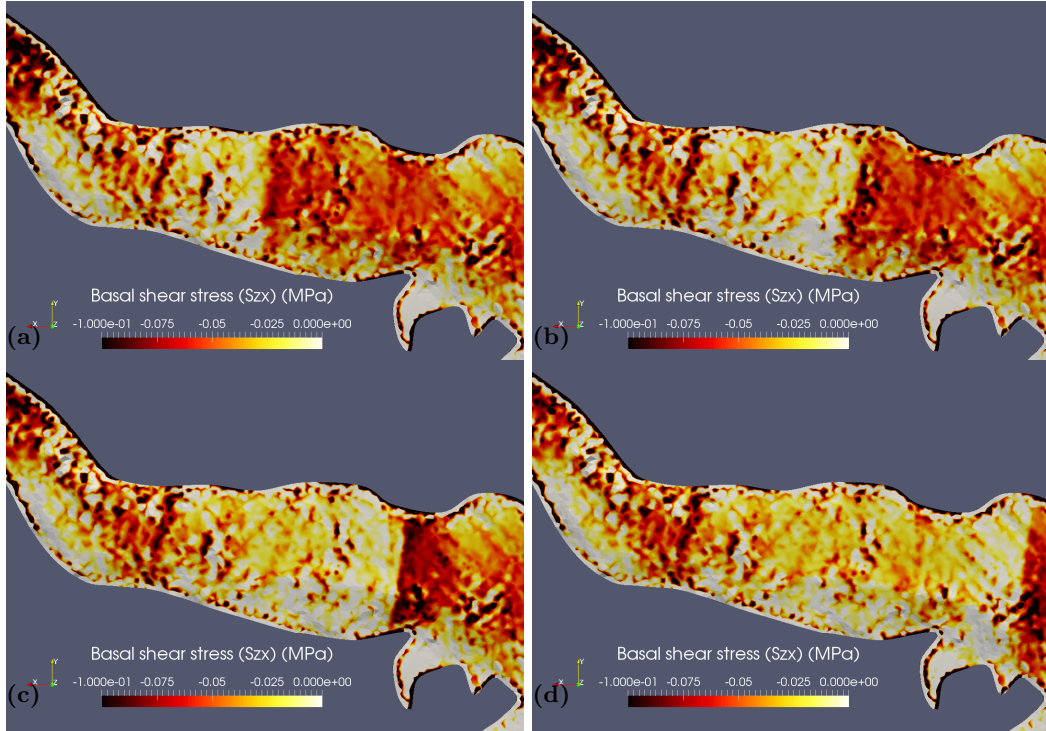


Figure 12. Modeled basal shear stress throughout a short surge simulation. Displayed is the basal shear stress that acts on the plane orthogonal to the z -axis in the direction of the x -axis. Note that we are viewing the glacier from the bottom, with the positive x -axis pointing to the left, unlike the other figures in this section where the glacier is viewed from above with the positive x -axis pointing to the right. Stress is given in units of mega-Pascals. (a) Basal shear stress at time step 10, (b) basal shear stress at time step 40, (c) basal shear stress at time step 80 and (d) basal shear stress at time step 132.

943 5.2.3 Elevation Change

944 Figure 13 shows elevation change throughout the surge simulation. Subfigure (a)
 945 gives the overall mass transfer near the beginning of the surge simulation to the end. In
 946 general, we see mass transfer from the upper trunk to the lower trunk, that is, from the
 947 areas affected by the surge to the down-glacier areas not yet affected (in terms of basal
 948 friction). We see elevation changes that exceed 50, and even 100 m, over the course of
 949 approximately 1 year, which is consistent with observations (U. C. Herzfeld et al., 2013;
 950 Burgess et al., 2013; Trantow & Herzfeld, 2016). Subfigure (b) gives the elevation change
 951 from time step 32 to time step 80, which shows that initial surface lowering in the ac-
 952 tivation zone ($\approx 3.9-4.0 \times 10^5$ UTM-East) is larger than at the end of the surge simula-
 953 tion when ice from further up-glacier flows into the evacuated region. Notably, we see
 954 that there are significant elevation changes far down glacier of the active region indicat-
 955 ing that regions away from the active surge zones are affected by the increased flow speeds
 956 long before the surge front reaches that area. Finally, subfigure (c) gives the elevation
 957 change from time step 80 to time step 132. This figure shows that surface lowering only
 958 occurs in the down-glacier half of the activation zone ($\approx 3.75-3.95 \times 10^5$ UTM-East) where
 959 surge speeds are the largest. The mass transfer to upper Bering comes from the lower

960 Bagley Ice Field, across the BBJ, which relives the mass-build up of that area (RA-64).
 961 Perhaps most notably, at each moment in time the location of the surge front is obvi-
 962 ous when looking at temporally-local elevation changes where the surface is actively low-
 963 ering behind the front and raising in front of it, which would resemble the oft identified
 964 “surge bulge”. We find that the overall spatiotemporal progression of elevation-change
 965 during the surge matches the observations derived from CryoSat-2 data as described in
 966 Trantow and Herzfeld (2016).

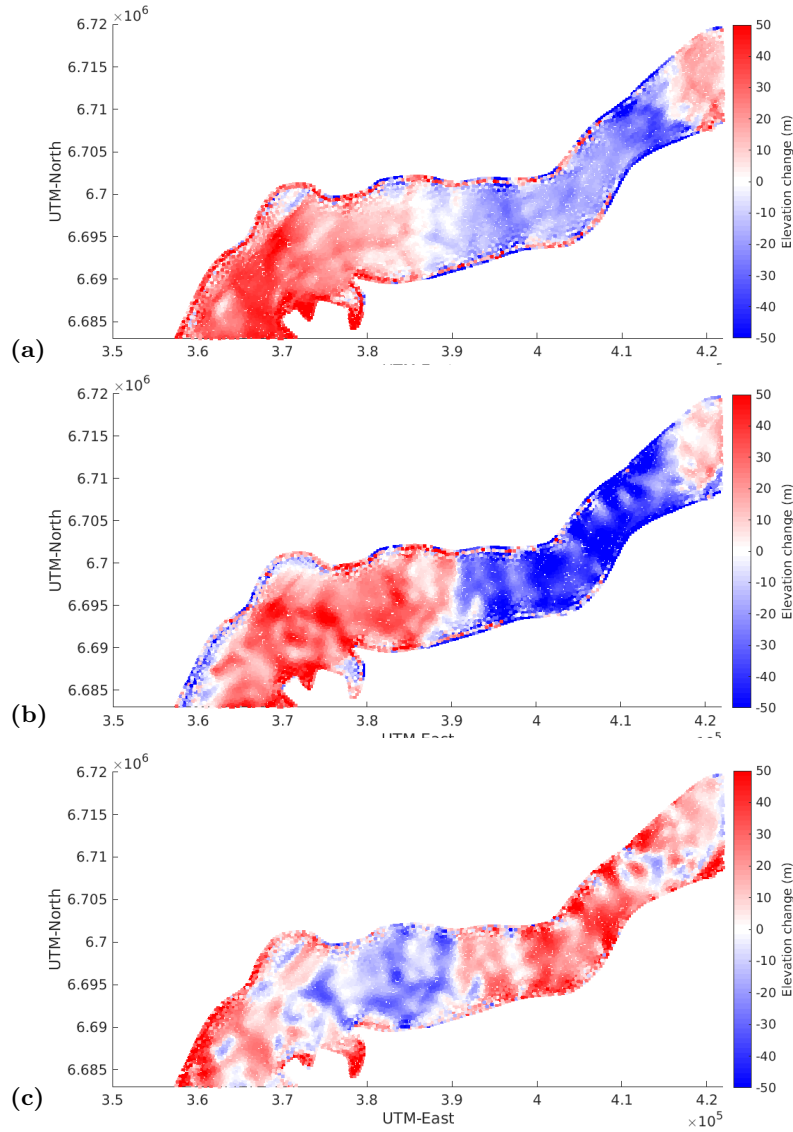


Figure 13. Modeled elevation change throughout a short surge simulation. Elevation change is given in units of meters. (a) Elevation difference between time 32 and time 132, (b) elevation difference between time 32 and time 80 and (c) elevation difference between time 80 and time 132.

967 **5.2.4 Hydropotential**

968 Finally, we take a look at the changing hydropotential and hydropotential gradi-
 969 ent along-flowline during the surge simulation. Figure 14 shows these quantities near the
 970 beginning of the surge (after time step 32, a half-year into the initial surge phase) and
 971 in the middle of the initial surge phase after the surge front has progressed 20 km down-
 972 glacier (time step 80 or Day-400 of the initial surge phase). The first aspect to note is
 973 the change in hydropotential in the surge activation zone (km-100 to km-120). The hy-
 974 drdraulic gradient has decreased throughout most of the activation zone implying that the
 975 passing surge wave, and the fast-sliding activation zone behind it, serves to further de-
 976 grade the efficiency of the basal drainage system.

977 Previous theories predict that the passing of the surge (or kinematic) wave would
 978 activate the switch from an EDS to an IDS (W. B. Kamb, 1987). However, we show here,
 979 and in the previous section, that the basal drainage system becomes less efficient through-
 980 out quiescence and becomes even more inefficient once the surge wave passes through.
 981 Our approach also does not require any assumption of a linked-cavity system. We also
 982 see that the small ($\sim 3\text{km}$) region centered at km-103 of positive hydraulic gradient, where
 983 water is predicted to collect, has shifted slightly down-glacier (indicated by an arrow in
 984 Figure 14(b)). This results implies that water accumulation areas may shift during the
 985 progression of the surge.

986 We also note that in the region up-glacier of the initiation location, the hydropo-
 987 tential “levels-out” with less variation along-flowline and a reduction in the estimated
 988 amount of basal water collection. This observation indicates that regions far up-glacier
 989 of the activation zone, which are modeled using the normal flow friction law value β_q ,
 990 are becoming more efficient in their basal drainage indicating a return to a quiescent state
 991 as mass is redistributed down-glacier during the surge.

992 **5.3 Second Surge Phase Analysis via Satellite Observations**

993 In this section, we use CryoSat-2 DEMs to derive observation-based hydropoten-
 994 tial maps of the BBGS during the 2011-2013 phase of the surge in order to infer drainage
 995 characteristics throughout the glacier during the peak of the surge in early-2011, when
 996 glacier velocities exceeded 22 m/day (Figure 15 (a)), and near the end of the surge in
 997 2013 when dynamic activity in Bering Glacier had reduced significantly (Figure 15 (b)),
 998 with velocities below 2 m/day in most of Lower and Central Bering. These velocity maps
 999 are derived using feature-tracking methods applied to Landsat-7 and Landsat-8 imagery
 1000 respectively. As seen in the early 2011 map, reliable velocity estimates are difficult to
 1001 attain while the glacier is surging, with features used in correlation rapidly deforming
 1002 over the course of several days (Trantow & Herzfeld, 2018). Moreover, the stripping in
 1003 Landsat-7 imagery (Markham et al., 2004) greatly reduces the area for which ice-velocities
 1004 can be derived. The Landsat-8 imagery used in the 2013 map, together with the glacier
 1005 moving much slower, provides better overall velocity estimates for the BBGS. We note
 1006 however, that the Sentinel-1 SAR imagery, available beginning in 2014, provide the most
 1007 reliable and comprehensive velocity estimates (e.g., Figure 10(a)) due to the fact that
 1008 SAR imagery is not complicated by the presence of clouds.

1009 The CryoSat-2 satellite began providing reliable glacier height measurements around
 1010 the start of the 2011-phase of the BBGS surge. As shown in Trantow and Herzfeld (2016),
 1011 we can derive ice surface DEMs, and thus unique hydropotential maps, every six months
 1012 from the CryoSat-2 data. Therefore, we can estimate hydropotential based on CryoSat-
 1013 2 surface elevation observations rather than from modeled BBGS surface height as we
 1014 have done previously. Figures 15(c) and (d) compare the CryoSat-2-estimated basal hy-
 1015 dropotential for Summer 2011 (May 2011-October 2011) during the main acceleration
 1016 phase and Summer 2013 (May 2013-October 2013) once most of the major surge activ-

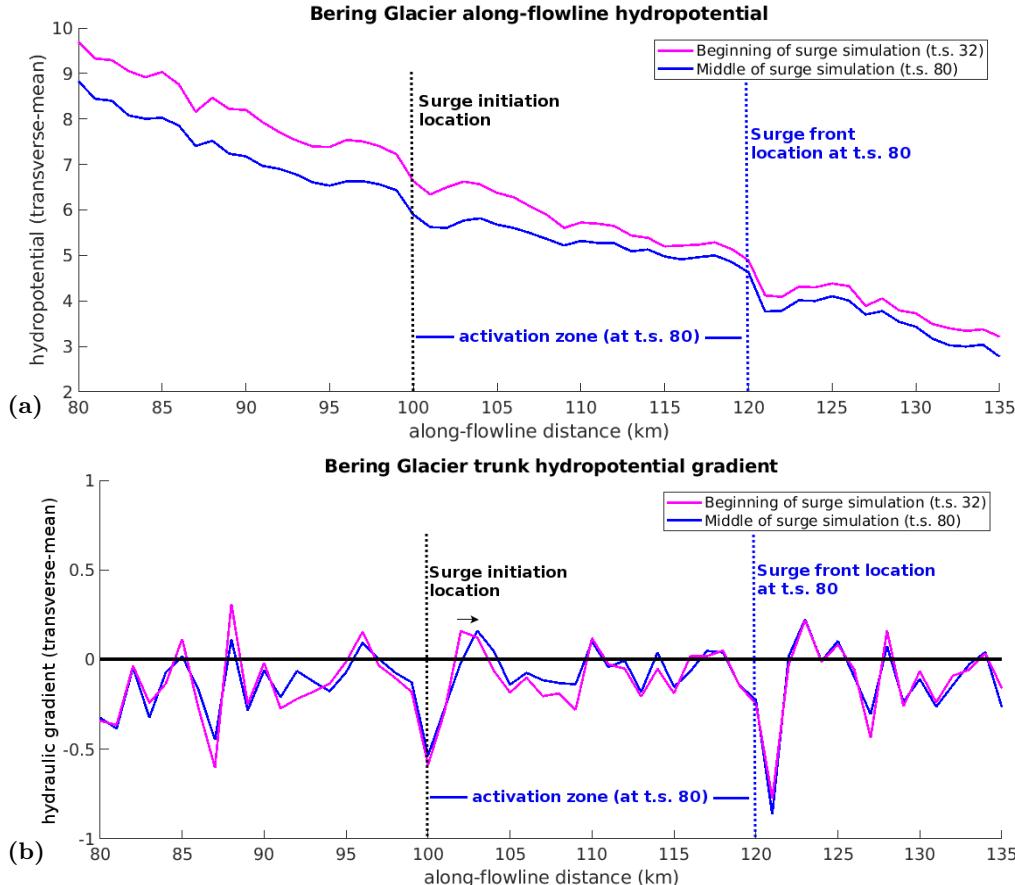


Figure 14. Hydropotential and hydraulic gradient during the surge simulation.

The magenta curves correspond to the glacier state near the beginning of the surge at time step 32 (Day-160) and the blue lines correspond to the glacier state after the surge wave has propagated 20 km down-glacier at time step 80 (Day-400). Labeled are the surge initiation location along-flowline (black dotted line) and the surge front location along-flowline at time step 80 (blue dashed line). (a) Modeled hydropotential (MPa) and (b) modeled hydraulic gradient ($\frac{MPa}{km}$). The small black arrow indicates the shift of a water accumulation zone down-glacier during the surge.

1017
1018
1019
1020
1021
1022
1023
1024
1025
ity in Bering Glacier had ceased. In Summer 2013, the hydropotential begins to better
resemble the bed topographical potential and becomes less dominated by ice over bur-
den pressure, with less water dispersing transversely and increased water drainage ef-
ficiency down-glacier. Looking at Bering Glacier's trunk, we see the contour lines become
more evenly spaced and more transversely aligned in 2013. This indicates that a more
steady, down-glacier flow, i.e. efficient flow, has manifested after the surge had ended by
2013 (in Central-Bering Glacier). We also see a reduction in the amount of hydropoten-
tial wells throughout the trunk indicating less capacity to store water beneath the glacier
by the end of the surge.

1026
1027
1028
1029
1030
These observations suggest that the transition from an IDS to an EDS begins at
the glacier terminus, sometime between 2012 and 2013, and propagates up-glacier un-
til it reaches the Bering-Bagley junction. The up-glacial surface velocity slowdown in the
assumed IDS regions during this time indicate that the down-glacier EDS is more effi-
ciently draining the up-glacial IDS, thus reducing basal water pressures there. Though,

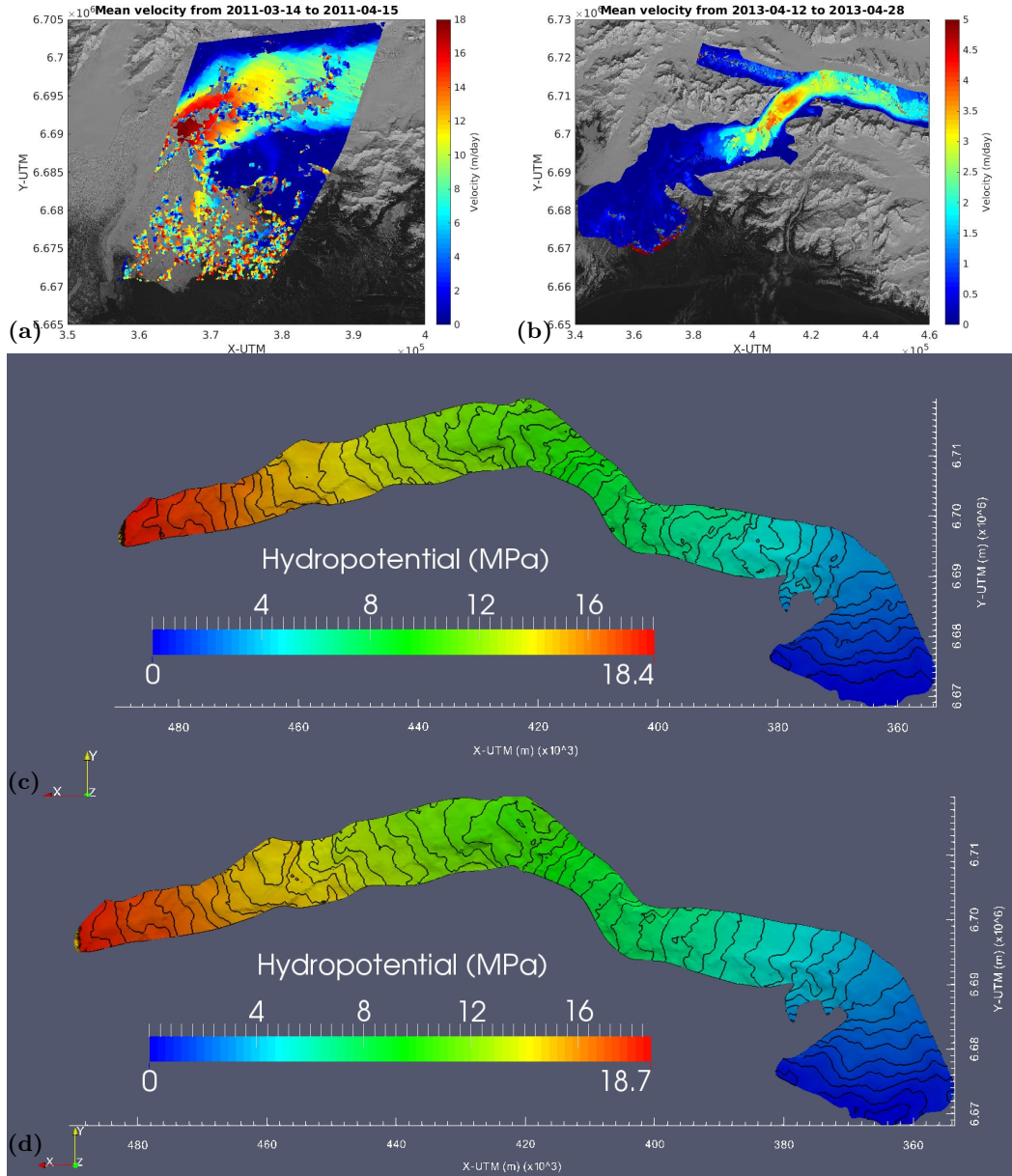


Figure 15. Velocity and basal hydropotential derived from observations during and after the surge in Bering Glacier. (a) Mean ice-surface velocity between 2011-03-14 and 2011-04-15 derived from Landsat-7 imagery. (b) Mean ice-surface velocity between 2013-04-12 and 2013-04-28 derived from Landsat-8 imagery. (b) Hydropotential derived from CryoSat-2 Baseline-C DEM for Summer 2011 (May 2011 - October 2011). (c) Hydropotential derived from CryoSat-2 Baseline-C DEM for Summer 2013 (May 2013 - October 2013). In conjunction with CryoSat-2 surface maps, both maps use the JPL-WISE bed topography maps in their estimation of hydropotential.

as we have shown in previous sections, the transition from an EDS to an IDS throughout quiescence is gradual and the drainage state is not simply binary. Therefore, we should expect the transition back to drainage efficiency to be somewhat gradual.

1034 **5.4 Observed Transition Back to Quiescence**

1035 In theory, after redistribution of mass throughout the glacier system, the glacier
 1036 returns once more to a stable geometry. Slowdowns in the Alaskan-type surge-glacier sys-
 1037 tems are usually correlated with large outburst floods at the glacier terminus (W. Kamb
 1038 et al., 1985), and the subglacial drainage system returns to an efficient one. This tran-
 1039 sition typically begins at the front of the glacier and slowly moves up-glacier until the
 1040 entire glacier system returns to an EDS. This process is reflected by observed velocity
 1041 at the cessation of the surge. The derived velocity map in Figure 15(b) from 2013 shows
 1042 that low velocities (less than 1 m/day) exist in Lower Bering while higher velocities (2-
 1043 5 m/day) remain in Upper Bering and the Bagley Ice Field. From 2012 onwards, the re-
 1044 gion of fast flow shrinks to only the Bagley Ice Field, with peak velocities also decreas-
 1045 ing (Trantow, 2020). The highest velocities in 2013 remain in the Bagley Ice Field and
 1046 just below the Bering-Bagley junction where basal slopes are high. By the year 2016,
 1047 the entire glacier system is moving at less than 1 m/day, and effects of the recent surge
 1048 have disappeared entirely, with the whole system in a state of low basal pressures and
 1049 efficient drainage (Figure 10(a)).

1050 **6 Summary and Conclusions**

1051 In this paper, we utilized numerical simulations, supplemented by satellite and air-
 1052 borne observations, to investigate dynamic, geometric and hydraulic aspects of both the
 1053 quiescent and surge phases of the Bering-Bagley Glacier System, Alaska. The analysis
 1054 centers on inter-annual changes of mass redistribution throughout the glacier system and
 1055 its implications on water drainage via calculation of hydropotential.

1056 The quiescent phase simulation shows a steepening of local geometry, retainment
 1057 of water and slowed-drainage paths that build throughout Bering Glacier's trunk lead-
 1058 ing to prime surging conditions. These results are mostly attributed to the particular
 1059 properties of the bedrock topography. The most significant features are a series of sub-
 1060 glacial ridges, which are extensions of the surrounding mountains beneath the glacier.
 1061 These subglacial ridges lead to damming of ice and water over the course of quiescence.
 1062 The build-up of ice at the subglacial ridges forms reservoir areas that slow down-glacier
 1063 drainage in the areas directly up-glacier and can even lead to water retainment in the
 1064 closest 2-4 km at several locations (specified in Figures 8 and 9). The simulation of the
 1065 quiescent phase shows an increase of stored water in Bering Glacier's trunk by a factor
 1066 of 2.46 over 20 years of evolution, which is estimated by calculating the positive hydraulic
 1067 gradient area (shaded regions in Fig 8).

1068 Moreover, the changing geometry during quiescence slows the overall down-glacier
 1069 drainage through Bering Glacier's trunk through increased transverse water paths caused
 1070 by the various ice dams. The difference in hydropotential across Bering's trunk, from
 1071 km-80 to km-135, decreased 16.6% after 20 years of quiescent flow. The increasing amount
 1072 of stored water and slowed down-glacier drainage lead to evermore water in the subglacial
 1073 drainage system at a given time leaving the glacier primed for surging. While surge and
 1074 quiescent phases are modeled in separate simulations, we propose a surge initiation cri-
 1075 terion that is based on the inferred amount of stored water based on the hydropoten-
 1076 tial calculation.

1077 Based on an observed surge wave in the BBGS, we propose a surge-wave friction
 1078 law to simulate the initial surge phase through Bering Glacier's main trunk. Modeled
 1079 velocities were consistent with those observed during the early stages of the latest surge
 1080 in the BBGS from 2008 through 2010. Our results show that while changes in basal con-
 1081 ditions are initially concentrated within an activation zone, as prescribed by the evolv-
 1082 ing friction law, significant basal shear stress and elevation changes occur throughout the

1083 glacier system indicating that effects from an initial surge acceleration can be seen to
 1084 propagate both up- and down-glacier of the surge initiation area.

1085 As the simulated surge front moves down-glacier, we find that the drainage efficiency
 1086 further decreases within the active surging area. Glacier geometry begins to level out
 1087 after ice in the reservoir areas is transferred to the receiving areas. Analysis of hydropo-
 1088 tential maps, derived from CryoSat-2 altimeter data, indicates that the drainage system
 1089 of the BBGS shows characteristics of a return to an efficient drainage system, where down-
 1090 glacier flow dominates and hydropotential wells disappear.

1091 In summary, our model of the BBGS captures key characteristics of the surge cy-
 1092 cle including peak velocities, building reservoir areas and mass transfer. The bedrock to-
 1093 graphy DEM is an important component of the model's ability to capture observed
 1094 spatial qualities of the glacier dynamics such as locations of reservoir areas and veloc-
 1095 ity patterns. Model physics were kept relatively simple as a first order attempt to recre-
 1096 ate observed surge behaviors and we have proposed places where increased complexity
 1097 could improve modeled results. This includes utilization of the hydropotential estimates
 1098 for improving the uniform liner friction law used in quiescence, and also the surge-wave
 1099 friction law.

1100 7 Open Research

1101 The Solver Input Files (SIF) for the Elmer/Ice simulations performed in this anal-
 1102 ysis, along with the Bering Glacier specific datasets and User Functions (USF), are avail-
 1103 able in the first author's GitHub repository:

1104 https://github.com/trantow/bbgs_elmer.

1105 Sentinel-1 SAR data are freely available at the Copernicus Open Access Hub:
 1106 <https://scihub.copernicus.eu/>

1107 The Sentinel Application Platform (SNAP) (Veci et al., 2014), used in this project
 1108 to derive velocity maps, is also freely available for download at:
 1109 <https://step.esa.int/main/download/snap-download/>

1110 Acknowledgments

1111 We would like to thank Dr. Ralf Greve (Institute of Low Temperature Science, Hokkaido
 1112 University, Sapporo, Japan) for his invaluable input in our understanding of ice-dynamic
 1113 modeling and for co-advising the first author in the research pertaining to this paper.
 1114 We thank Eric Rignot (Jet Propulsion Laboratory, Pasadena, USA and University Cal-
 1115 ifornia Irvine, USA) and Jeremie Mouginot (University California Irvine, USA) for shar-
 1116 ing their bed topographic data of the BBGS and Veit Helm (Alfred Wegener Institute,
 1117 Bremen, Germany) for sharing their CryoSat-2 TFMRA-swath data for the BBGS. Sup-
 1118 port of this research through the U.S. National Science Foundation's Office of Polar Pro-
 1119 grams (Awards OPP-1745705 and OPP-1942356), Office of Advanced Cyberinfrastruc-
 1120 ture (Award OAC-1835256), Arctic Natural Sciences Program (Award ARC-1148800)
 1121 and Geography and Spatial Sciences (Award GSS-1553133), and through NASA Cryospheric
 1122 Sciences (Award NNX17AG75G) is gratefully acknowledged (U. Herzfeld is the PI of all
 1123 awards).

1124 References

1125 Benn, D., Fowler, A. C., Hewitt, I., & Sevestre, H. (2019). A general theory of
 1126 glacier surges. *Journal of Glaciology*, 65(253), 701–716.
 1127 Björnsson, H. (1974). *Explanations of jökulhlaups from Grímsvötn, Vatnajökull, Ice-*

1128 *land.*

1129 Björnsson, H. (1998). Hydrological characteristics of the drainage system beneath a
1130 surging glacier. *Nature*, 395(6704), 771.

1131 Boulton, G., Lunn, R., Vidstrand, P., & Zatsepin, S. (2007). Subglacial drainage
1132 by groundwater-channel coupling, and the origin of esker systems: part 1-
1133 glaciological observations. *Quaternary Science Reviews*, 26(7-8), 1067–1090.

1134 Brinkerhoff, D. J., Meyer, C. R., Bueler, E., Truffer, M., & Bartholomaus, T. C.
1135 (2016). Inversion of a glacier hydrology model. *Annals of Glaciology*, 57(72),
1136 84–95.

1137 Burgess, E. W., Forster, R. R., Larsen, C. F., & Braun, M. (2013). Surge Dynamics
1138 on Bering Glacier, Alaska, in 2008–2011. *The Cryosphere*, 6, 1251–1262.

1139 Chu, W., Schroeder, D. M., Seroussi, H., Creyts, T. T., Palmer, S. J., & Bell, R. E.
1140 (2016). Extensive winter subglacial water storage beneath the Greenland Ice
1141 Sheet. *Geophysical Research Letters*, 43(24), 12–484.

1142 Clarke, G. K., Collins, S. G., & Thompson, D. E. (1984). Flow, thermal structure,
1143 and subglacial conditions of a surge-type glacier. *Canadian Journal of Earth
1144 Sciences*, 21(2), 232–240.

1145 Cuffey, K., & Paterson, W. S. B. (2010). *The Physics of Glaciers* (4th ed.). Else-
1146 vier.

1147 de Fleurian, B., Werder, M. A., Beyer, S., Brinkerhoff, D. J., Delaney, I., Dow,
1148 C. F., ... others (2018). SHMIP The subglacial hydrology model intercompar-
1149 ison Project. *Journal of Glaciology*, 64(248), 897–916.

1150 Eisen, O., Harrison, W., Echelmeyer, K., Bender, G., & J.Gorda. (2005). Variegated
1151 Glacier, Alaska, USA: A century of surges. *Journal of Glaciology*, 51, 399–406.

1152 Fatland, D., Lingle, C., & Truffer, M. (2003). A surface motion survey of Black
1153 Rapids Glacier, Alaska, U.S.A. *Annals of Glaciology*, 36, 29–36.

1154 Fatland, D. R., & Lingle, C. S. (1998). Analysis of the 1993–95 Bering Glacier
1155 (Alaska) surge using differential SAR interferometry. *Journal of Glaciology*,
1156 44(148), 532–546.

1157 Fatland, D. R., & Lingle, C. S. (2002). InSAR observations of the 1993–95 Bering
1158 Glacier (Alaska, USA) surge and a surge hypothesis. *Journal of Glaciology*,
1159 48(162), 439–451.

1160 Fleischer, P. J., Bailey, P. K., Natel, E. M., Muller, E. H., Cadwell, D. H., & Rus-
1161 sell, A. (2010). The 1993–1995 surge and foreland modification, Bering Glacier,
1162 Alaska. *Geological Society of America Special Paper*(462), 193–216.

1163 Fleurian, B. d., Gagliardini, O., Zwinger, T., Durand, G., Meur, E. L., Mair, D.,
1164 & Råback, P. (2014). A double continuum hydrological model for glacier
1165 applications. *The Cryosphere*, 8(1), 137–153.

1166 Flowers, G. E., & Clarke, G. (2002a). A multicomponent coupled model of
1167 glacier hydrology, 1, Theory and synthetic examples. *Journal Geophys. Res.*,
1168 107(B11), 2287. doi: 10.1029/2001JB001122

1169 Flowers, G. E., & Clarke, G. (2002b). A multicomponent coupled model of glacier
1170 hydrology, 2, Application to Trapridge Glacier, Yukon, Canada. *Journal Geo-
1171 phys. Res.*, 107(B11), 2288. doi: 10.1029/2001JB001124

1172 Fowler, A. (1987). A theory of glacier surges. *Journal of Geophysical Research: Solid
1173 Earth* (1978–2012), 92(B9), 9111–9120.

1174 Fowler, A. (1989). A mathematical analysis of glacier surges. *SIAM J. Appl. Math.*,
1175 49(1), 246–263.

1176 Gagliardini, O., Zwinger, T., Gillet-Chaulet, F., Durand, G., Favier, L., Fleurian,
1177 B. d., ... others (2013). Capabilities and performance of Elmer/Ice, a new-
1178 generation ice sheet model. *Geoscientific Model Development*, 6(4), 1299–
1179 1318.

1180 Greve, R., & Blatter, H. (2009). *Dynamics of Ice Sheets and Glaciers*. Berlin, Ger-
1181 many etc.: Springer. doi: 10.1007/978-3-642-03415-2

1182 Gully, J., Benn, D., Screamton, E., & Martin, J. (2009). Mechanisms of englacial con-

duit formation and their implications for subglacial recharge. *Quaternary Science Reviews*, 28(19-20), 1984–1999.

Gulley, J., Grabiec, M., Martin, J., Jania, J., Catania, G., & Glowacki, P. (2012). The effect of discrete recharge by moulin and heterogeneity in flow-path efficiency at glacier beds on subglacial hydrology. *Journal of Glaciology*, 58(211), 926–940.

Harrison, W., & Post, A. (2003). How much do we really know about glacier surging? *Annals of Glaciology*, 36(1), 1–6.

Heinrichs, T. A., Mayo, L., Echelmeyer, K., & Harrison, W. (1996). Quiescent-phase evolution of a surge-type glacier: Black Rapids Glacier, Alaska, USA. *Journal of Glaciology*, 42(140), 110–122.

Helm, V., Humbert, A., & Miller, H. (2014). Elevation and elevation change of Greenland and Antarctica derived from CryoSat-2. *The Cryosphere*, 8(4), 1539–1559.

Herzfeld, U. (1998). *The 1993-1995 surge of bering glacier (Alaska) — a photographic documentation of crevasse patterns and environmental changes* (Vol. 17). Geograph. Gesellschaft Trier and Fachbereich VI – Geographie/Geowissenschaften, Universität Trier.

Herzfeld, U. C. (2004). *Atlas of Antarctica: Topographic maps from geostatistical analysis of satellite radar altimeter data* (Vol. 1). Springer Verlag.

Herzfeld, U. C., & Mayer, H. (1997). Surge of Bering Glacier and Bagley Ice Field, Alaska: an update to August 1995 and an interpretation of brittle-deformation patterns. *Journal of Glaciology*, 43(145), 427–434.

Herzfeld, U. C., McDonald, B., Stachura, M., Hale, R. G., Chen, P., & Trantow, T. (2013). Bering Glacier surge 2011: Analysis of laser altimeter data. *Annals of Glaciology*, 54(63), 158–170. doi: 10.3189/2013AoG63A348

Humphrey, N. F., & Raymond, C. (1994). Hydrology, erosion and sediment production in a surging glacier: Variegated Glacier, Alaska, 1982–83. *Journal of Glaciology*, 40(136), 539–552.

Jay-Allemand, M., Gillet-Chaulet, F., Gagliardini, O., & Nodet, M. (2011a). Investigating changes in basal conditions of Variegated Glacier prior to and during its 1982–1983 surge. *The Cryosphere*, 5(3), 659–672.

Jay-Allemand, M., Gillet-Chaulet, F., Gagliardini, O., & Nodet, M. (2011b). Investigating changes in basal conditions of Variegated Glacier prior to and during its 1982–1983 surge. *The Cryosphere*, 5(3), 659–672. Retrieved from <http://www.the-cryosphere.net/5/659/2011/> doi: 10.5194/tc-5-659-2011

Jiskoot, H. (1999). Characteristics of surge-type glaciers. *Ph.D. thesis*, 1–262.

Josberger, E. G., Shuchman, R. A., Meadows, G. A., Savage, S., & Payne, J. (2010). Hydrography and circulation of ice-marginal lakes at Bering Glacier, Alaska, USA. *Geological Society of America Special Paper*(462), 67–82.

Kamb, B. (1970). Sliding motion of glaciers: theory and observation. *Reviews of Geophysics*, 8(4), 673–728.

Kamb, W., Raymond, C., Harrison, W., Engelhardt, H., Echelmeyer, K., Humphrey, N., ... Pfeffer, T. (1985). Glacier surge mechanism: 1982–1983 surge of Variegated Glacier, Alaska. *Science*, 227(4686), 469–479.

Kamb, W. B. (1987). Glacier Surge Mechanism Based on Linked Cavity Configuration of the Basal Water Conduit System. *Journal Geophys. Res.*, 92(B9), 9083–9100.

Koehler, R., & Carver, G. (2018). Active faults and seismic hazards in Alaska. *Alaska Div. Geol. Geophys. Surv., Miscellaneous Publication* 160.

Larour, E., Utke, J., Csatho, B., Schenk, A., Seroussi, H., Morlighem, M., ... Khazendar, A. (2014). Inferred basal friction and surface mass balance of North-East Greenland Ice Stream using data assimilation of ICESat-1 surface altimetry and ISSM. *The Cryosphere Discussions*, 8(3), 2331–2373. Retrieved from <http://www.the-cryosphere-discuss.net/8/2331/2014/> doi: 10.5194/tcd-8-2331-2014

10.5194/tcd-8-2331-2014

1238 Larsen, C., Burgess, E., Arendt, A., O'neel, S., Johnson, A., & Kienholz, C. (2015).
 1239 Surface melt dominates Alaska glacier mass balance. *Geophysical Research Letters*, 42(14), 5902–5908.

1240 LeBlanc, L. (2009). *Icequakes and ice motion: A time-series analysis of the dynamics of the Bering Glacier, Alaska* (Unpublished doctoral dissertation). University of Alaska Fairbanks.

1241 Lingle, C., & Fatland, D. (2003). Does englacial water storage drive temperate glacier surges? *Annals of Glaciology*, 36, 14–20.

1242 Lingle, C., Post, A., Herzfeld, U. C., Molnia, B. F., Krimmel, R., & Roush, J. (1993). Bering Glacier surge and iceberg-calving mechanism at Vitus Lake, Alaska, USA. *Journal of Glaciology*, 39, 722–727.

1243 Lliboutry, L. (1968). General theory of subglacial cavitation and sliding of temperate glaciers. *Journal of Glaciology*, 7, 21–58.

1244 Magnússon, E., Björnsson, H., Rott, H., & Pálsson, F. (2010). Reduced glacier sliding caused by persistent drainage from a subglacial lake. *The Cryosphere*, 4(1), 13–20.

1245 Markham, B. L., Storey, J. C., Williams, D. L., & Irons, J. R. (2004). Landsat sensor performance: History and current status. *IEEE Transactions on Geoscience and Remote Sensing*, 42(12), 2691–2694.

1246 Mayer, H., & Herzfeld, U. (2000). Structural glaciology of the fast-moving Jakobshavn Isbræ, Greenland, compared to the surging Bering Glacier, Alaska, USA. *Annals of Glaciology*, 30(1), 243–249.

1247 Meier, M., & Post, A. (1969). What are glacier surges? *Canadian Journal of Earth Sciences*, 6(4), 807–817.

1248 Molnia, B., & Post, A. (1995). Holocene history of Bering Glacier, Alaska: A prelude to the 1993–1994 surge. *Physical Geography*, 16(2), 87–117.

1249 Molnia, B., & Williams, R. (2001). *Glaciers of Alaska* (Vol. 28-2). Alaska Geographic Society.

1250 Molnia, B. F. (2008). *Alaska*. Washington, D.C.: U.S. Geological Survey Professional Paper 1386-K.

1251 Molnia, B. F., & Post, A. (2010). Introduction to the Bering Glacier system, Alaska/Canada: Early Observations and scientific investigations, and key geographic features. *Geological Society of America Special Paper*(462), 13–42.

1252 Murray, T. (1997). Assessing the paradigm shift: deformable glacier beds. *Quaternary Science Reviews*, 16(9), 995–1016.

1253 Murray, T., Strozzi, T., Luckman, A., Jiskoot, H., & Christakos, P. (2003). Is there a single surge mechanism? Contrasts in dynamics between glacier surges in Svalbard and other regions. *Journal of Geophysical Research: Solid Earth*, 108(B5).

1254 Post, A. (1972). Periodic surge origin of folded medial moraines on Bering Piedmont Glacier, Alaska. *Journal of Glaciology*, 11(62), 219–226.

1255 Raymond, C. (1987). How do glaciers surge? A review. *Journal of Geophysical Research*, 92(B9), 9121–9134.

1256 Raymond, C. (1988). Evolution of Variegated Glacier, Alaska, USA, prior to its surge. *J. Glaciol.*, 34(117), 154–169.

1257 Raymond, C., Benedict, R., Harrison, W., Echelmeyer, K., & Sturm, M. (1995). Hydrological discharges and motion of Fels and Black Rapids Glaciers, Alaska, USA: implications for the structure of their drainage systems. *Journal of Glaciology*, 41(138), 290–304.

1258 Raymond, C., Johannesson, T., Pfeffer, T., & Sharp, M. (1987). Propagation of a glacier surge into stagnant ice. *Journal of Geophysical Research: Solid Earth*, 92(B9), 9037–9049.

1259 Rignot, E., Mouginot, J., Larsen, C., Gim, Y., & Kirchner, D. (2013). Low-frequency radar sounding of temperate ice masses in Southern Alaska. *Geo-*

1293 *physical Research Letters*, 40(20), 5399–5405.

1294 Robin, G. d. Q. (1969). Initiation of glacier surges. *Canadian Journal of Earth Sci-*
1295 *ences*, 6(4), 919–928.

1296 Robin, G. d. Q., & Weertman, J. (1973). Cyclic surging of glaciers. *Journal of*
1297 *Glaciology*, 12(64), 3–18.

1298 Roush, J. J., Lingle, C. S., Guritz, R. M., Fatland, D. R., & Voronina, V. A. (2003).
1299 Surge-front propagation and velocities during the early-1993-95 surge of
1300 Bering Glacier, Alaska, U.S.A., from sequential SAR imagery. *Annals of*
1301 *Glaciology*, 36, 37–44.

1302 Sevestre, H., Benn, D. I., Hulton, N. R., & Bælum, K. (2015). Thermal structure of
1303 Svalbard glaciers and implications for thermal switch models of glacier surging.
1304 *Journal of Geophysical Research: Earth Surface*, 120(10), 2220–2236.

1305 Sharp, M., Richards, K., Willis, I., Arnold, N., Nienow, P., Lawson, W., & Tison,
1306 J.-L. (1993). Geometry, bed topography and drainage system structure of the
1307 haut glacier d'arolla, switzerland. *Earth Surface Processes and Landforms*,
1308 18(6), 557–571.

1309 Shoemaker, E. (1986). Subglacial hydrology for an ice sheet resting on a deformable
1310 aquifer. *J. Glaciol.*, 32(110), 20–30.

1311 Shoemaker, E., & Leung, H. (1987). Subglacial drainage for an ice sheet resting
1312 upon a layered deformable bed. *Journal of Geophysical Research: Solid Earth*,
1313 92(B6), 4935–4946.

1314 Shreve, R. (1972). Movement of water in glaciers. *Journal of Glaciology*, 11(62),
1315 205–214.

1316 Shuchman, R., & Josberger, E. G. (2010). Bering Glacier: Interdisciplinary Stud-
1317 ies of Earth's Largest Temperate Glacier. *Geological Society of America Special*
1318 *Paper*(462), 384.

1319 Shuchman, R. A., Josberger, E. G., Jenkins, L. K., Payne, J. F., Hatt, C. R., &
1320 Spaete, L. (2010). Remote sensing of the Bering Glacier region. *Geological*
1321 *Society of America Special Paper*(462), 43–66.

1322 Tangborn, W. (2013). Mass balance, runoff and surges of Bering Glacier, Alaska.
1323 *The Cryosphere*, 7(3), 867–875.

1324 Trantow, T. (2014). *Numerical experiments of dynamical processes during the*
1325 *2011-2013 surge of the Bering-Bagley Glacier System, using a full-Stokes finite*
1326 *element model* (Unpublished master's thesis). University of Colorado.

1327 Trantow, T. (2020). *Surging in the bering-bagley glacier system, alaska – under-*
1328 *standing glacial acceleration through new methods in remote sensing, numerical*
1329 *modeling and model-data comparison* (Unpublished doctoral dissertation).
1330 University of Colorado.

1331 Trantow, T., & Herzfeld, U. (2016). Spatiotemporal mapping of a large mountain
1332 glacier from CryoSat-2 altimeter data: surface elevation and elevation change
1333 of Bering Glacier during surge (2011-2014). *International Journal of Remote*
1334 *Sensing*, 0-28. doi: 10.1080/01431161.2016.1187318

1335 Trantow, T., & Herzfeld, U. C. (2018). Crevasses as indicators of surge dynam-
1336 ics in the Bering Bagley Glacier System, Alaska: Numerical experiments and
1337 comparison to image data analysis. *Journal of Geophysical Research: Earth*
1338 *Surface*. doi: 10.1029/2017JF004341

1339 Trantow, T., Herzfeld, U. C., Helm, V., & Nilsson, J. (2020). Sensitivity of glacier
1340 elevation analysis and numerical modeling to cryosat-2 sral retracking tech-
1341 niques. *Computers & Geosciences*, 104610.

1342 Truffer, M., Harrison, W. D., & Echelmeyer, K. A. (2000). Glacier motion dom-
1343 inated by processes deep in underlying till. *Journal of Glaciology*, 46(153),
1344 213–221.

1345 Turrin, J., Forster, R. R., Larsen, C., & Sauber, J. (2013). The propagation of
1346 a surge front on Bering Glacier, Alaska, 2001-2011. *Annals of Glaciology*,
1347 54(63).

1348 Veci, L., Prats-Iraola, P., Scheiber, R., Collard, F., Fomferra, N., & Engdahl, M.
1349 (2014). The Sentinel-1 toolbox. In *Proceedings of the ieee international geo-*
1350 *science and remote sensing symposium (igarss)* (pp. 1–3).
1351 Weertman, J. (1972). General theory of water flow at the base of a glacier or ice
1352 sheet. *Reviews of Geophysics*, 10(1), 287–333.